MANCHESTER 1824
The University of Manchester

The University of Manchester Research

A dual-mesh hybrid RANS-LES simulation of the buoyant flow in a differentially heated square cavity with an improved resolution criterion

DOI:
10.1016/j.compfluid.2021.104949

Document Version
Accepted author manuscript

Link to publication record in Manchester Research Explorer

Citation for published version (APA):
Emad Abdelmagid Ali, A., Afgan, I., Laurence, D., & Revell, A. (2021). A dual-mesh hybrid RANS-LES simulation of the buoyant flow in a differentially heated square cavity with an improved resolution criterion. *Computers & Fluids*. https://doi.org/10.1016/j.compfluid.2021.104949

Published in:
Computers & Fluids

Citing this paper
Please note that where the full-text provided on Manchester Research Explorer is the Author Accepted Manuscript or Proof version this may differ from the final Published version. If citing, it is advised that you check and use the publisher's definitive version.

General rights
Copyright and moral rights for the publications made accessible in the Research Explorer are retained by the authors and/or other copyright owners and it is a condition of accessing publications that users recognise and abide by the legal requirements associated with these rights.

Takedown policy
If you believe that this document breaches copyright please refer to the University of Manchester's Takedown Procedures [http://man.ac.uk/04Y6Bo] or contact uml.scholarlycommunications@manchester.ac.uk providing relevant details, so we can investigate your claim.

OPEN ACCESS

Download date:08. Jun. 2022

A dual-mesh hybrid RANS-LES simulation of the buoyant flow in a differentially heated square cavity with an improved resolution criterion

Abdelmagid Emad Abdelmagid Ali[1], Imran Afgan[2,1], Dominique Laurence[1] and Alistair Revell[1]

[1]Department of Mechanical, Aerospace and Civil Engineering, School of Engineering, The University of Manchester, George Begg Building, Sackville Street, Manchester M13 9PL, UK

[2]Department of Mechanical Engineering, School of Engineering, Khalifa University, Abu Dhabi, P.O. Box 127788, United Arab Emirates

Corresponding author: Abdelmagid Emad Abdelmagid Ali

Email address: abdelmajid24@windowslive.com

Present work address: Department of Mechanical, Aerospace and Civil Engineering, School of Engineering, The University of Manchester, George Begg Building, Sackville Street, Manchester M13 9PL, UK

Keywords: Hybrid RANS/LES, Buoyant flow, Differentially heated cavity, LES resolution, OpenFOAM

Highlights:

- A hybrid RANS/LES simulation of a $Ra = 10^{11}$ square cavity flow was run using OpenFOAM.
- The new criterion distinguishes between the viscous sublayer and the laminar core.
- The new criterion leads to sustained turbulence levels in the dual-mesh simulation.

Abstract

In this work, the dual-mesh hybrid RANS-LES approach was applied for the first time to a natural convection flow, namely a high Rayleigh number differentially heated square cavity flow. This approach involves running an unsteady Reynolds Averaged Navier-Stokes (RANS) simulation and a coarse Large Eddy Simulation (LES) simultaneously using two different grids that overlap each other (typically, a highly wall-refined grid is used for the RANS, whereas a more homogenous and isotropic mesh is used for the LES). The two simulations correct each other using a switching criterion that determines the driving and the driven simulations at every point in space. It is demonstrated that the flow unsteadiness and the coexistence of laminar and turbulent regions in the square cavity complicate the task of choosing a suitable switching criterion. Accordingly, a new criterion based on comparing the turbulence lengthscales to the grid size was developed to account for the presence of the aforementioned complex flow features. The behaviour of this criterion and comparisons of the dual-mesh predictions against pure RANS, pure coarse LES and Direct Numerical Simulation (DNS) results are also presented in the current paper.

1. Introduction

The buoyancy driven flow in a heated cavity is a key benchmark for many civil or power-generation engineering applications such as solar collectors or passive safety nuclear plant designs. One important difference between the square and the tall buoyant cavities is that the former features a stronger stable stratification that results in significant damping of turbulence. As a result, the Rayleigh number required for the transition to turbulence is higher in the square cavity than in a tall cavity. According to Henkes & Le Quéré (1996) and Xin & Le Quéré (2001), the critical Rayleigh number at which transition to turbulence occurs in a square cavity configuration with perfectly conducting horizontal walls is of the order of 10^6. On the other hand, the Rayleigh numbers of the flow in the cavity with a 28:1 aspect ratio (with height =28*width) studied experimentally by Betts & Bokhari (2000) were $0.86 * 10^6$ and $1.43 * 10^6$ and the flow was fully turbulent. Wall-resolved Large Eddy Simulation (LES) or Direct Numerical Simulation (DNS) such as Sebilleau (2016), Wu et al. (2017a), Wu et al. (2017b), Wu et al. (2019), Benhamadouche et al. (2020) and Ahmed et al. (2020) are very expensive for high Reynolds and/or Rayleigh number flows as it requires a very fine mesh in the near-wall regions in all three directions to resolve the turbulence structures.

Hybrid RANS-LES methods can provide a cheaper way of computing the square cavity flow compared to LES, Revell et al. (2020). In these hybrid methods, the near-wall region is handled by the RANS model which allows wall normal refinement with high-aspect ratio cells that are at odds with LES theory. The dual-mesh hybrid RANS-

LES technique used in this work was developed by Xiao & Jenny (2012) for isothermal flows and a number of improvements were suggested by Tunstall et al. (2017) and Tunstall (2016) who also extended the idea of the approach to heat transfer problems.

In previous studies of the square cavity in the literature, separate LES and RANS works can be found. Peng & Davidson (2001) performed an LES study for a Rayleigh number of $1.58 * 10^9$. For this Rayleigh number the levels of the turbulence in the cavity are relatively low. The dynamic Smagorinsky model yielded good predictions of the mean quantities of the flow and thermal fields despite the fact that some discrepancies were observed in the prediction of the second moments.

One example of a RANS study of the square cavity can be found in Omranian et al. (2014) where both eddy viscosity and Reynolds stress models were used with different turbulent heat flux models. In addition, different near-wall treatments were tested, namely the low Reynolds-number treatment, the standard wall function (which is based on the logarithmic velocity distribution) and the analytical wall function (see Craft et al. (2002)).

As regards hybrid RANS-LES simulations of the square cavity flow, Abramov & Smirnov (2006) studied the case at a Rayleigh number of $1.58 * 10^9$ using a Detached Eddy Simulation (DES) based on the one equation model that solves for the turbulent kinetic energy. The predictions of the mean flow and thermal fields were reasonable. However, close to the downstream ends of the vertical walls, the authors observed an under-prediction of the vertical walls' boundary layer thickness and an overprediction of the vertical velocity peaks in these boundary layers. Another hybrid RANS-LES study can be found in Kocutar et al. (2015), where the boundary elements method was used to study both laminar and turbulent natural convection.

Most of the studies found in the literature are limited to low Rayleigh numbers, as there was a lack of experimental and DNS data for high Rayleigh numbers. In fact, until recently the maximum Rayleigh number reported in experiments and in DNS studies was of the order of 10^9 which can be found in Ampofo & Karayiannis (2003) and Puragliesi & Leriche (2012), respectively. However, Sebilleau (2016) conducted DNS studies in which the Rayleigh numbers were 10^8, $1.58 * 10^9$, 10^{10} and 10^{11}. The author generated fine DNS data (was later published in Sebilleau et al. (2018)) which he used to perform an extensive analysis of different RANS closure techniques. The present work utilizes this DNS data to shed some light on whether hybrid RANS-LES can provide an alternative to both LES and RANS for simulating high Rayleigh number square cavity flows.

The organisation of this paper is as follows. The second section provides an explanation of the square cavity configuration studied here. The third section gives insight into the dual-mesh approach by explaining both the flow and the heat transfer related parts of the method. This section also briefly mentions the RANS and the LES models that were chosen to conduct this work. The fourth section highlights the code and the discretization techniques that

were used here. The results obtained here are included in the fifth section which is followed by the concluding section.

2. The differentially heated square cavity

The square cavity test-case shown in Fig. 1 (with periodic boundary conditions in the z-direction to represent a cavity that is infinitely long in this direction) is computed for a Rayleigh number (Ra) of 10^{11}, a fluid Prandtl number (Pr) equal to 0.71 and a linear temperature boundary condition at the horizontal walls (i.e. the temperature varies linearly between the hot wall temperature (T_h) and the cold wall temperature (T_c)). This linear temperature variation represents the case of ''highly conductive'' horizontal walls more relevant to industrial components with thick steel walls. Note that Ra of 10^{11} is also industrially relevant (similar to a Reynolds number of 10^5).

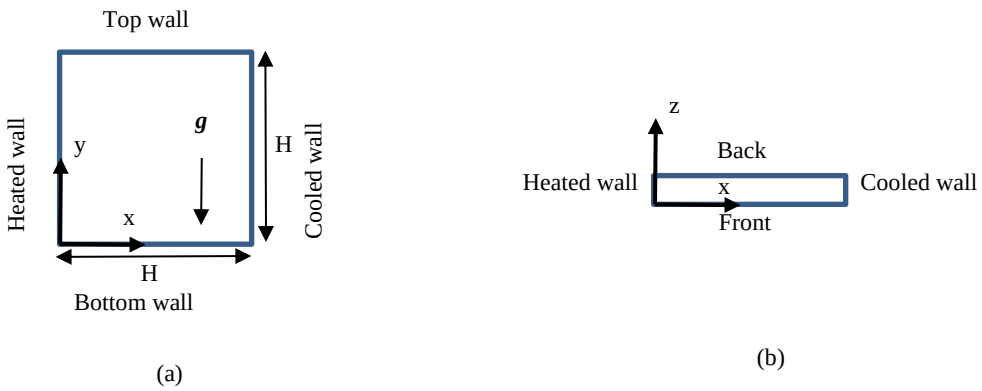

Fig. 1. Schematic representation of different cross sections of the buoyant square cavity. $\boldsymbol{g}$ is the gravity vector.

In this study, pure unsteady RANS, pure coarse LES and dual-mesh hybrid RANS-LES simulations were run and the results were compared to the DNS data of Sebilleau et al. (2018). The LES and RANS meshes were both generated using STARCCM+ v11.02 in which the available hyperbolic tangent grid stretching function was used when creating the two grids. The length of the domains in the spanwise direction was chosen to be $0.15\ H$, where H is the cavity height as in the DNS study of Sebilleau et al. (2018) who checked the decay of two-point correlations.

The RANS mesh consists of 250*250*1 cells with near-wall grid spacing of 0.0002 H. The same near-wall grid spacing was used in the RANS simulations of Sebilleau (2016) and it allows the near-wall nodes to be located within the viscous sublayer. Using a finer RANS grid was found to have little impact on the results.

On the other hand, the LES mesh has 150*150*23 cells with near-wall grid spacing of 0.003137 H. The LES mesh had to be refined in the wall normal direction because of the small thickness of the boundary layers. However, the grid is still too coarse for the LES to fully resolve the near-wall region. Indeed, using the local DNS wall shear

stress values, the average value of x^+ ($x^+ = \frac{x\sqrt{\frac{\tau_w}{\rho}}}{\nu}$, where x is the wall-distance of the near-wall node and τ_w, ρ and ν are the wall shear stress, fluid density and kinematic viscosity, respectively) over the hot wall is approximately 14. Note that x^+ better represents this quantity compared to y^+, since the direction normal to the hot wall here is the x direction. The local values of this parameter as well as Δy^+ and Δz^+ ($\Delta y^+ = \frac{\Delta y\sqrt{\frac{\tau_w}{\rho}}}{\nu}$ and $\Delta z^+ = \frac{\Delta z\sqrt{\frac{\tau_w}{\rho}}}{\nu}$, where Δy and Δz are the near-wall grid spacings in the y and z directions, respectively) over the hot wall are shown in Fig. 2.

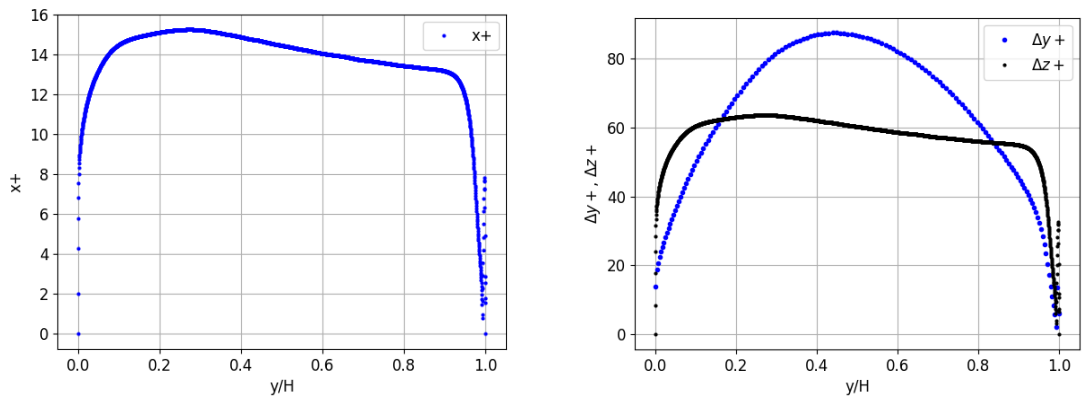

(a) (b)

Fig. 2. Local values of x^+ (shown in (a)), Δy^+ and Δz^+ (both are shown in (b)) along the hot wall. These values were estimated using the local wall shear stress from the DNS data of Sebilleau (2016). H is the cavity height. y was used here to represent the vertical distance from the bottom wall.

The LES mesh of 0.5 million cells plus the negligible cost of the RANS simulation provide enormous economy compared to the 726 million nodes DNS simulation.

3. Methodology

3.1. The dual-mesh approach

In the dual-mesh approach, two computational domains are overlapped, one of these domains is used to solve the RANS equations and in the other domain, LES equations are solved. The two solutions are "nudged" together on the fly similarly to two-phase flow modelling where drift terms couple the fields of both phases, here the RANS and the time averaged LES fields, which could be imagined as high and low inertia phases respectively, e.g. solid particles in gas flow in the two fluid model of Zhang & Reese (2003).

The advantage of this overlapping flow-models approach is that it avoids the interface problem that occurs with single-mesh hybrid methods that try to match the highly fluctuating LES quantities with the smooth RANS ensemble-averaged quantities. On the other hand, in the dual-mesh approach the RANS quantities are compared to corresponding LES quantities that are averaged in time. Following Xiao & Jenny (2012), the averaging operator here is an Exponentially Weighted Averaging operation $\langle \quad \rangle^{EWA}$:

$$\langle \phi \rangle^{\mathrm{EWA}}(t) = \int_{-\infty}^{t} \phi\,(t') \frac{1}{T_{avg}} exp\left(-\frac{(t-t')}{T_{avg}}\right) dt' \qquad (1)$$

where ϕ can be any variable, t denotes the current point in time, t′ represents times that precede the current time, T_{avg} is the averaging time scale.

A first order approximation of this operation allows the exponentially weighted averaged (EWA) quantities to be estimated as:

$$\langle \phi \rangle^{EWA,n} = (1-\alpha)\phi^{n} + \alpha \langle \phi \rangle^{EWA,n-1} \qquad (2)$$

where n represents the current time step, $n-1$ refers to the previous time step and $\alpha = \frac{1}{1+\frac{\Delta t}{T_{avg}}}$ in which Δt is the time step size.

3.1.1. Consistency of the flow fields

In the dual-mesh approach, the classic RANS and LES momentum equations, with Boussinesq approximation for density variation and eddy viscosity models for turbulent stresses, are supplemented with the “drift force” source terms Q^R and Q^L:

$$\frac{\partial \langle U_i \rangle}{\partial t} + \langle U_j \rangle \frac{\partial \langle U_i \rangle}{\partial x_j} = -\frac{1}{\rho_{ref}} \frac{\partial \langle p \rangle}{\partial x_i}$$

$$+ \frac{\partial}{\partial x_j}\left((\nu + \nu_t)\left(\frac{\partial \langle U_i \rangle}{\partial x_j}\right)\right)$$

$$+ (1 - \beta\left(\langle T \rangle - T_{ref}\right) g_i$$

$$+ {Q_i}^{R} \qquad (3)$$

$$\frac{\partial \overline{U}_i}{\partial t} + \overline{U}_j \frac{\partial \overline{U}_i}{\partial x_j} = -\frac{1}{\rho_{ref}} \frac{\partial \overline{p}}{\partial x_i}$$

$$+ \frac{\partial}{\partial x_j}\left(\left(\nu + \nu_{sgs}\right) \left(\frac{\partial \overline{U}_i}{\partial x_j}\right)\right)$$

$$+ (1 - \beta \left(\overline{T} - T_{ref}\right) g_i$$

$$+ Q_i^{L,u} + Q_i^{L,g} \qquad (4)$$

where the angle brackets $\langle \quad \rangle$ and the overbar $\overline{\quad}$ denote Reynolds averaged and spatially filtered quantities, respectively, ν_t is the RANS eddy viscosity and ν_{sgs} is the sgs viscosity. β is the thermal expansion coefficient and T_{ref} and ρ_{ref} represent the reference temperature and reference density, respectively. The drift terms are defined as:

$$Q_i^R = \sigma^L \frac{\langle \overline{U}_i \rangle^{EWA} - \langle U_i \rangle}{\gamma_{r1}} \qquad (5)$$

$$Q_i^{L,u} = (1 - \sigma^L) \left(\frac{\langle U_i \rangle - \langle \overline{U}_i \rangle^{EWA}}{\gamma_{l1}} \right) \qquad (6)$$

$$Q_i^{L,g} = (1 - \sigma^L) \left(\frac{G_i}{\gamma_{l2}} \right) \qquad (7)$$

where γ_{r1}, γ_{l1} and γ_{l2} are timescales that control how fast the solutions relax towards each other and G_i is a function of the resolved LES velocity fluctuation.

The drift term added to the RANS momentum equation (Q_i^R in Equation (3)) drives the RANS velocity field towards the EWA LES velocity field where the LES is superior to the RANS (far from the walls). On the other hand, the source term in the LES momentum equation ($Q_i^{L,u}$ in Equation (4)) acts to modify the LES velocity field in a way that makes the LES EWA velocity field consistent with the RANS velocity field at locations where one knows that the RANS performs better than the LES (near the walls).

The switch function σ^L takes values 0 or 1 (depending on whether the RANS drives the LES or vice versa) in most of the domain except in a narrow model-transition layer, the position and width of which is defined by the specific choice of the σ^L function. Its choice depends on the user-chosen or affordable LES grid. This re-opens the large research topic of quality criteria for LES (Salvetti et al. (2010)) and will be revisited in section 5.2.

To disconnect LES mesh requirements from viscous scaling and avoid the difficult buffer layer resolution, i.e. to start trusting the LES only in the fully turbulent Log-layer, Tunstall et al. (2017) specified the interface below which the RANS drives the LES and above which the LES drives the RANS as the location where the quantity $Re_y = \frac{\sqrt{k^R} y}{\nu}$ equals 200:

$$\sigma^{L} = 0.5\left(1 + \tanh\left(\frac{Re_y - 200}{10}\right)\right) \qquad (8)$$

k^R is the RANS turbulent kinetic energy, y is the wall distance and ν is the kinematic viscosity.

Similar to the velocity fields, the total turbulent kinetic energies of the RANS and the LES are made consistent by the addition of source terms to the momentum and turbulence equations. In regions where the LES is under resolved, the source term ${Q_i}^{L,g}$ (in Equation (4)) adjusts the LES resolved fluctuations to make the LES total (EWA) turbulent kinetic energy (k^{EWA}) equal to the RANS turbulent kinetic energy (k^R). In order to enhance this consistency in regions where the contribution of the modelled turbulent kinetic energy to the total turbulent kinetic energy is significant, Tunstall et al. (2017) decided to adjust the subgrid-scale (sgs) turbulent kinetic energy k_{sgs} through the addition of a source term ($Q^{k_{sgs}}$) to the k_{sgs} transport equation (Equation (11)), which is solved when using the one equation k LES model. The function G_i in Equation (7) reads:

$$G_i = \left(1 - \frac{{k_{sgs}}^{EWA}}{k^{EWA}}\right)\frac{k^R - k^{EWA}}{k^R + k^{EWA}}(\bar{U}_i - \langle\bar{U}_i\rangle^{EWA}) \qquad (9)$$

$$k^{EWA} = \langle 0.5\, {u_i}''\, {u_i}''\rangle^{EWA} + {k_{sgs}}^{EWA} \qquad (10)$$

where k_{sgs} is the sgs turbulent kinetic energy, ${u_i}'' = \overline{U_i} - \langle\overline{U_i}\rangle^{EWA}$ is the resolved LES velocity fluctuation and k^{EWA} is the EWA total LES turbulent kinetic energy. The LES sgs k equation reads:

$$\frac{\partial k_{sgs}}{\partial t} + \frac{\partial}{\partial x_j}\left(k_{sgs}\bar{U}_j\right) = 2\nu_{sgs}\overline{S_{ij}}^2 + \frac{\partial}{\partial x_j}\left(\nu_{sgs}\frac{\partial k_{sgs}}{\partial x_j}\right) - \varepsilon_{sgs} + G_{ksgs} + Q^{k_{sgs}} \qquad (11)$$

$$Q^{k_{sgs}} = (1 - \sigma^{L})\frac{{k_{sgs}}^{EWA}}{k^{EWA}}\frac{k^R - k^{EWA}}{\gamma_{r2}} \qquad (12)$$

where ε_{sgs} and $\overline{S_{ij}}$ are the sgs dissipation rate and the filtered strain rate tensor, respectively. G_{ksgs} is a buoyancy production term (see Appendix B).

On the other hand, in regions where the LES is well resolved, the RANS turbulent kinetic energy is forced towards the LES "total EWA turbulent kinetic energy" by modifying the turbulent kinetic energy production term in the RANS turbulence equations as shown in Equation (13).

$$P_k = {P_k}^{model} + \sigma^{L}\frac{k^{EWA} - k^R}{\gamma_{r2}} \qquad (13)$$

where P_k is the modified RANS turbulent kinetic energy production term and ${P_k}^{model}$ represents the original

RANS turbulence production term. The quantities γ_{l1}, γ_{l2} , γ_{r1} and γ_{r2} are called the relaxation time scales and are defined as:

$$\gamma_{l1} = \gamma_{r1} = max\left(C_{\gamma 1}\frac{k^R}{\varepsilon^R}, \Delta t\right) \tag{14}$$

$$\gamma_{l2} = \gamma_{r2} = max\left(C_{\gamma 2}\frac{k^R}{\varepsilon^R}, \Delta t\right) \tag{15}$$

where ε^R is the RANS turbulence dissipation rate, $C_{\gamma 1} = 0.1$ and $C_{\gamma 2} = 0.01$.

Even though the forcing of the turbulence levels of the LES towards the RANS turbulence levels described above only enforces consistency between the total turbulent kinetic energies, one can choose to make all the components of the LES total turbulent stress tensor consistent with their RANS counterparts instead. A drift term formulation that can accomplish this consistency can be found in Xiao & Jenny (2012) who pointed out that the stress consistency would be better justified when the estimated RANS turbulent stress tensor can be trusted (e.g. when using a Reynolds stress model) compared to when using an eddy viscosity model.

Another drift term that enforces the stress consistency was suggested by de Laage de Meux et al. (2015) in the framework of anisotropic linear forcing for the generation of turbulence near the inlet of an LES domain. The authors added a drift term to the LES momentum equation to drive the LES mean velocity and resolved stresses towards target RANS velocity and stresses provided by a RANS simulation that used the elliptic blending Reynolds stress model (see Manceau & Hanjalić (2002)). However, the same forcing strategy used by the authors can be used in the dual-mesh framework.

It is also worth noting that some dual-mesh methods proposed in the literature enforce the consistency between the LES and the RANS not via a relaxation forcing but in implicit ways that effectively correct the LES total turbulent stresses. More details about these methods can be found in Xiao et al. (2016) and Nguyen et al. (2020). Furthermore, another dual-mesh method was suggested by Davidson (2019) in which the author coupled a DES solution with a steady RANS solution and the coupling strategy involved using relaxation forcing.

3.1.2. Consistency of the thermal fields

Regarding the thermal fields, Tunstall (2016) decided to achieve the consistency between the RANS and the LES fields by ensuring consistency between the RANS temperature and the LES EWA temperature as well as making the LES total EWA temperature variance consistent with the RANS temperature variance. Consequently, when using the dual-mesh approach to solve heat transfer problems one needs to solve transport equations for the RANS temperature variance and the LES sgs temperature variance where the later gives the modelled part of the

LES total temperature variance.

By using an eddy-diffusivity hypothesis to model the heat flux, the RANS and LES temperature equations read, respectively:

$$\frac{\partial\langle T\rangle}{\partial t}+\langle U_j\rangle\frac{\partial\langle T\rangle}{\partial x_j}=\frac{\partial}{\partial x_j}\left(\left(\frac{\nu}{Pr}+\frac{\nu_t}{Pr_t}\right)\frac{\partial\langle T\rangle}{\partial x_j}\right)+Q^{\langle T\rangle} \quad (16)$$

$$\frac{\partial\overline{T}}{\partial t}+\overline{U}_j\frac{\partial\overline{T}}{\partial x_j}=\frac{\partial}{\partial x_j}\left(\left(\frac{\nu}{Pr}+\frac{\nu_{sgs}}{Pr_{sgs}}\right)\frac{\partial\overline{T}}{\partial x_j}\right)+Q^{\overline{T}} \quad (17)$$

For both the turbulent Prandtl number Pr_t and the sgs Prandtl number Pr_{sgs} a value of 0.9 was used in this study. The drift terms in the above temperature equations are defined as:

$$Q^{\overline{T}}=(1-\sigma^{L})\frac{\langle T\rangle-\langle\overline{T}\rangle^{EWA}}{\gamma_{l3}}+(1-\sigma^{L})\left(1-\frac{\Theta^{EWA}{}_{sgs}}{\Theta^{EWA}}\right)\frac{\Theta^{R}-\Theta^{EWA}}{\Theta^{R}+\Theta^{EWA}}\frac{\overline{T}-\langle\overline{T}\rangle^{EWA}}{2\gamma_{l4}} \quad (18)$$

$$Q^{\langle T\rangle}=\sigma^{L}\frac{\langle\overline{T}\rangle^{EWA}-\langle T\rangle}{\gamma_{r3}} \quad (19)$$

where $\Theta^{EWA}{}_{sgs}=\langle\overline{T'^{2}{}_{sgs}}\rangle^{EWA}$ is EWA of the LES sgs temperature variance and Θ^{EWA} is the EWA total LES temperature variance defined as $\Theta^{EWA}=\langle(\overline{T}-\langle\overline{T}\rangle^{EWA})^{2}+\overline{T'^{2}{}_{sgs}}\rangle^{EWA}$. $\Theta^{R}=\langle T'^{2}\rangle$ is the RANS temperature variance.

In regions where the LES is expected to be under-resolved, the mean temperature of the LES is modified by a source term that is added to its transport equation (Equation (17)). This source term is the first part of $Q^{\overline{T}}$ (defined in Equation (18)) and it increases or decreases the LES temperature to match the LES EWA temperature with the RANS temperature. At the other locations, the RANS temperature is driven towards the LES EWA temperature through the drift term $Q^{\langle T\rangle}$ in the RANS temperature equation (Equation (16)).

As regards the temperature fluctuations, at locations where the LES is under-resolved, both the resolved and modelled temperature fluctuations of the LES are adjusted to drive the EWA total LES temperature variance towards the RANS temperature variance. The resolved temperature fluctuations are modified by the second part of the source term $Q^{\overline{T}}$ (see Equation (18)) in the LES temperature equation (Equation (17)) and the modelled

temperature fluctuations are altered by adding a source term ($Q^{\overline{T'^2}_{sgs}}$) to the sgs temperature variance transport equation:

$$\frac{\partial \overline{T'^2}_{sgs}}{\partial t} + \bar{U}_j \frac{\partial \overline{T'^2}_{sgs}}{\partial x_j} =$$

$$2\left(\frac{\nu}{Pr} + \frac{\nu_{sgs}}{Pr_{sgs}}\right)\frac{\partial \bar{T}}{\partial x_i}\frac{\partial \bar{T}}{\partial x_i} - \frac{1}{Pr}\frac{\varepsilon^L}{k_{sgs}}\overline{T'^2}_{sgs}$$

$$+\frac{\partial}{\partial x_j}\left(\left(\frac{\nu}{Pr} + \frac{\nu_{sgs}}{Pr_{sgs}}\right)\frac{\partial \overline{T'^2}_{sgs}}{\partial x_j}\right) + Q^{\overline{T'^2}_{sgs}} \qquad (20)$$

where:

$$Q^{\overline{T'^2}_{sgs}} = (1 - \sigma^L)\frac{\Theta^{EWA}{}_{sgs}}{\Theta^{EWA}}\frac{\Theta^R - \Theta^{EWA}}{\gamma_{l4}} \qquad (21)$$

and

$$\varepsilon^L = 2\nu\overline{S_{ij}}\,\overline{S_{ij}} + \nu_{sgs}\overline{S_{ij}}\,\overline{S_{ij}} \qquad (22)$$

On the other hand, at locations where the LES is well-resolved, the RANS temperature variance is relaxed towards the EWA total LES temperature variance by the term $Q^{\langle T'^2\rangle}$ in the RANS temperature variance equation:

$$\frac{\partial\langle T'^2\rangle}{\partial t} + \langle U_j\rangle\frac{\partial\langle T'^2\rangle}{\partial x_j} = 2\frac{\nu_t}{Pr_t}\frac{\partial\langle T\rangle}{\partial x_i}\frac{\partial\langle T\rangle}{\partial x_i}$$

$$-\frac{1}{R_t}\frac{\varepsilon^R}{k^R}\langle T'^2\rangle + \frac{\partial}{\partial x_j}\left(\left(\frac{\nu}{Pr} + \frac{\nu_t}{Pr_t}\right)\frac{\partial\langle T'^2\rangle}{\partial x_j}\right)$$

$$+ Q^{\langle T'^2\rangle} \qquad (23)$$

where R_t (the thermal to dynamic time scales ratio) was set equal to 0.5 and the drift tem $Q^{\langle T'^2\rangle}$ reads:

$$Q^{\langle T'^2\rangle} = \sigma^L\frac{\Theta^{EWA} - \Theta^R}{\gamma_{r4}} \qquad (24)$$

The relaxation time scales of the thermal field read:

$$\gamma_{l3} = \gamma_{r3} = max\left(R_t C_{\gamma 1}\frac{k^R}{\varepsilon^R}, \Delta t\right) \qquad (25)$$

$$\gamma_{l4} = \gamma_{r4} = max\left(R_t C_{\gamma 2}\frac{k^R}{\varepsilon^R}, \Delta t\right) \qquad (26)$$

3.2. Turbulence models

The LES and RANS models used here are the one equation k model and the $BL\ v2/k$ model of Billard & Laurence (2012), respectively. The equations of the versions of these models that were used in this study are

provided in the Appendix. Details of the RANS model can be found in Billard and Laurence (2012), Uribe (2006), Hanjalić et al. (2004), Manceau et al. (2002) and Durbin (1991). The reader is also referred to Yoshizawa and Horiuti (1985) and Fureby et al. (1997) for details about the LES model.

4. Computational implementation and discretization techniques

All the simulations of this study were run in OpenFOAM 2.3.x using the dual-mesh code of Tunstall (2016). However, the heat transfer part of the dual-mesh formulation of Tunstall (2016) has been implemented as part of this work. Additionally, the dual-mesh code was combined with "buoyantBoussinesqPimpleFoam", which is an OpenFOAM solver for buoyant flows. The buoyancy related terms were also added to the equations of the RANS model.

A second-order accurate backwards scheme is used for the temporal discretization of both the RANS and the LES simulations. Regarding the spatial discretization, central differencing was used for the LES. On the other hand, the van Leer scheme (van Leer (1974)) was used for all the RANS equations with the exception of the momentum equation in which the second-order accurate upwind scheme was employed. The adjustable time step option in OpenFOAM was used to ensure that the Courant number remains less than 1. The pressure velocity coupling was handled using the PISO algorithm (Issa (1986)). The solver and the discretization procedures have been extensively tested and benchmarked over a variety of heat transfer and thermal hydraulics applications in the past, see Guleren et al. (2010), Han et al. (2012), Afgan et al. (2008), Kahil et al. (2019), Abed & Afgan (2017), Abed & Afgan (2020), Abed et al. (2020a), Abed et al. (2020b) and Benhamadouche et al. (2020).

5. Results

In the results presented here, the same nondimensionalization as the one chosen by Sebilleau et al. (2018) was used:

$$\mathbf{U} = \frac{\boldsymbol{U} HPr}{\nu\, Ra^{0.5}}\ ,\mathrm{T} = \frac{T - \left(\frac{T_h + T_c}{2}\right)}{\Delta T}\ ,\mathbf{x} = \frac{\boldsymbol{x}}{H} \qquad (27)$$

where $\boldsymbol{U}$ is the velocity vector, T is the temperature, $\boldsymbol{x}$ is the position vector, H is the cavity height and ΔT is the temperature difference: $T_h - T_c$. It should be noted that the terms'' hybrid RANS '' and ''hybrid LES'' are used for the RANS and the LES simulations that are run simultaneously when using the dual-mesh approach. On the other hand, what is meant by ''pure RANS'' and ''pure coarse LES'' are the RANS and coarse LES simulations that are run without being corrected and forced towards each other. The second moments of all the simulations reported in this section were calculated as the sum of their resolved and modelled components. For details about how this calculation can be done, the reader can refer to Sebilleau (2016).

Regarding the parameters of the dual-mesh method, the only parameter that needs to be chosen before the simulation which is the averaging period (T_{avg}) has been specified here as $32\frac{H}{\sqrt{g\beta H\Delta T}}$, where $\sqrt{g\beta H\Delta T}$ is a buoyant velocity scale (see for example Kumar & Dewan (2016) and Ammour et al. (2013)).

In section 5.1, the results obtained from the pure RANS and pure coarse LES simulations are reported. This allows the reader to get an idea of some of the shortcomings of these standalone simulations. In section 5.2, a new "resolution based" criterion for determining σ^{L} is suggested. Section 5.3 discusses the dual-mesh results obtained when σ^{L} was evaluated using the new criterion.

5.1. Pure RANS and pure coarse LES results:

Profiles of the mean velocity, total turbulent kinetic energy, total turbulent shear stress[1] and mean temperature from the pure RANS and pure coarse LES simulations are shown in Fig. 3-Fig. 5. All these statistics have been computed using the classic arithmetic mean operation (not to be confused with the EWA operation). It can be seen that the coarse LES predictions of the velocity and temperature are reasonable away from the wall. The LES predictions of the turbulent shear stress can be observed to improve towards the outer edge of the boundary layer. However, the coarse LES cannot be relied upon to provide wall parameters such as the Nusselt number and the wall shear stress.

[1] *It should be noted that the quantities called the total turbulent kinetic energy and the total turbulent shear stress do not only represent the fluctuations due to turbulence but also the fluctuations that are caused by mean flow instabilities.*

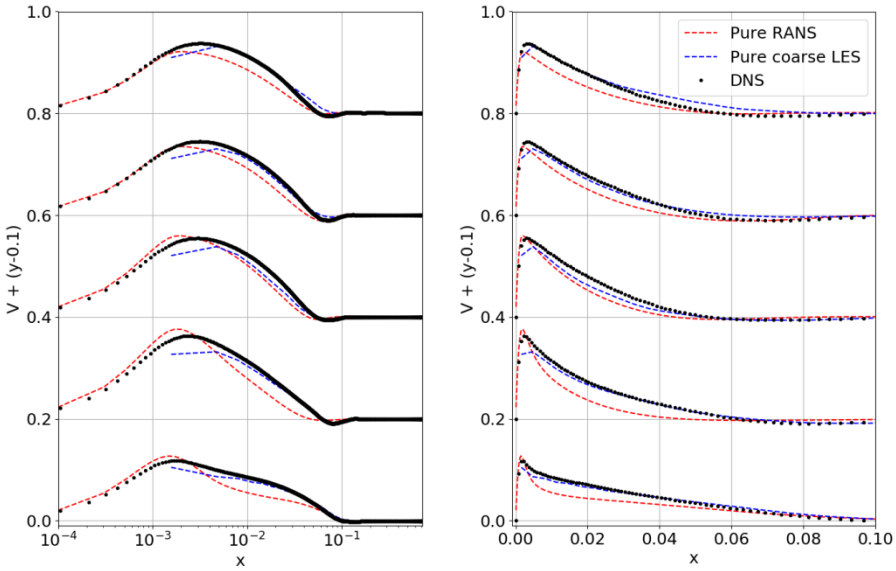

(a) (b)

Fig. 3. Plots showing the pure coarse LES and pure RANS predictions of the mean vertical velocity profiles near the hot wall at horizontal lines that correspond to cavity heights equal to $0.1H$, $0.3H$, $0.5H$, $0.7H$ and $0.9H$. (a) is a semi logarithmic plot (b) is a linear plot.

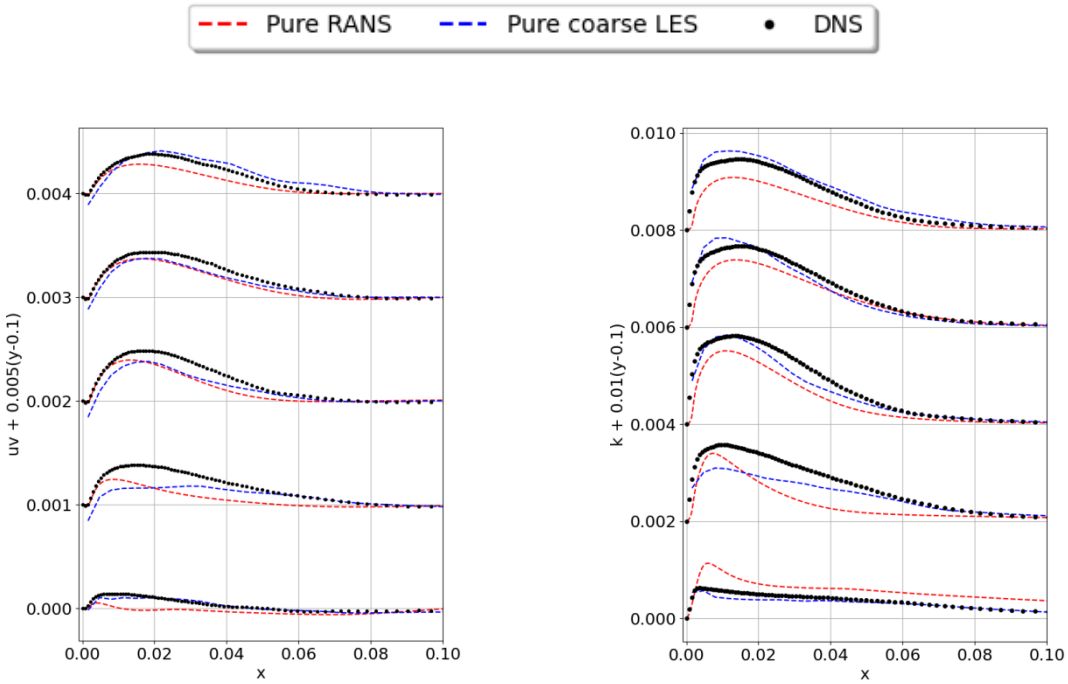

(a) (b)

Fig. 4. Plots showing the pure coarse LES and pure RANS predictions of the profiles near the hot wall at horizontal lines that correspond to cavity heights equal to $0.1H$, $0.3H$, $0.5H$, $0.7H$ and $0.9H$. (a) turbulent shear stress (b) total turbulent kinetic energy.

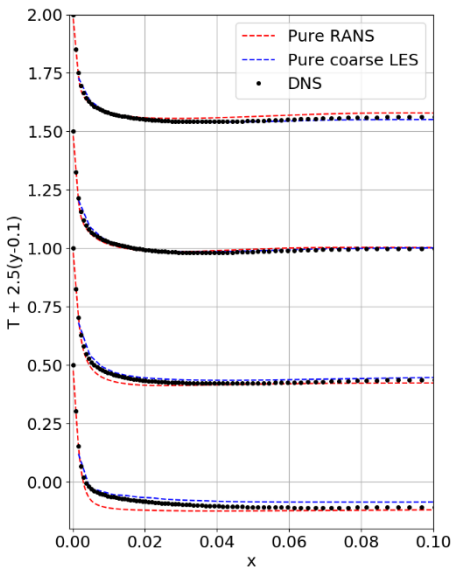

Fig. 5. A plot showing the pure coarse LES and pure RANS predictions of the mean temperature profiles near the hot wall at horizontal lines that correspond to cavity heights equal to $0.1H$, $0.3H$, $0.5H$ and $0.7H$.

The pure RANS predictions of the velocity profiles are unsatisfactory. At the heights of $0.1H$ and $0.3H$, the velocity in the immediate vicinity of the wall is overpredicted. This is because at these locations there is an underprediction of the wall normal mixing of wall parallel momentum clearly seen in the turbulent shear stress profiles at these locations (Fig. 4 (a)). The inadequate wall normal mixing of the RANS at y=$0.1H$ and $0.3H$ is consistent with the fact that the RANS underpredicts the thickness of the momentum boundary layer at the height of $0.3H$ as well as the width of the thermal boundary layer at both y=$0.1H$ and $0.3H$. At the vertical locations of $y = 0.7H$ and $0.9H$, the pure RANS seems to underpredict the velocity in the entire boundary layer. The total turbulent kinetic energy (TTKE) is underpredicted at all the locations apart from the height of $0.1H$ at which the RANS overpredicts the TTKE. The pure coarse LES predictions of the TTKE are in better agreement with the reference DNS data than the pure RANS.

One important thing to note is that this flow features the presence of unstably stratified flow regions particularly near the top right and bottom left corners. This unstable stratification is caused by the linear temperature profile at the horizontal walls. As explained by Sebilleau et al. (2018), this unstable stratification causes the appearance of buoyant plumes which rise along the hot wall and fall along the cold wall. This instability is the main reason why turbulence levels in this cavity are greater than what the turbulence levels would be in a cavity with horizontal walls that are adiabatic at the same Rayleigh number. These large turbulence levels can be observed in Fig. 6 in which a snapshot of the velocity field of the pure coarse LES simulation is shown.

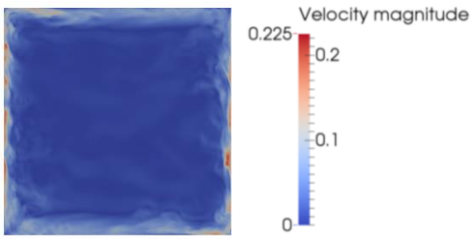

Fig. 6. An instantaneous snapshot of the LES velocity magnitude from the pure coarse LES simulation.

The high turbulence levels and the instabilities present in this flow are the reasons why no problem regarding the transition of the flow to a turbulent state was faced when the one-equation k model was used even though this model is dissipative and the LES grid is coarse. The same LES model was one of the models used by Kumar & Dewan (2016) in their wall-resolved LES study of the square cavity. The temperature variation imposed by the authors at the horizontal walls is likely to be the reason why no transition problem was reported. On the other hand, Barhaghi & Davidson (2007) experienced a transition delay problem when using the Smagorinsky model (which is also dissipative) to simulate a tall buoyant cavity which can be attributed to the adiabatic condition at

the horizontal walls of the cavity. Contrarily, the authors attained a good transition prediction with the dynamic Smagorinsky model.

Snapshots of the instantaneous temperature fields from the pure RANS and pure coarse LES simulations are shown in Fig. 7 and Fig. 8. In order to well visualize the aforementioned instability, a closer view of the flow near the bottom left corner is provided for both the pure RANS and the pure coarse LES temperature snapshots. In the RANS zoomed-in view, the unstable stratification that triggers the instability can be clearly seen near the bottom wall. This stratification increases from right to left (following the flow direction) until it is strong enough to allow the instability to form. It can be observed that the onset location of the pure coarse LES instability is upstream of the location where the RANS instability starts. However, the RANS instability appears to have a larger lengthscale than the LES instability. This might be the reason why the RANS predicts a high TTKE at the height of $0.1H$ since at this location the RANS resolved variances are significantly greater than the modelled variances. The dominance of the RANS resolved component of the TTKE over the modelled one in the boundary layer was observed to almost vanish near the midheight of the cavity.

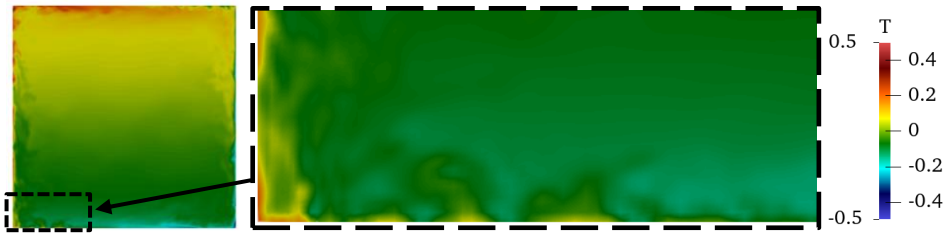

Fig. 7. An instantaneous snapshot of the temperature from the pure coarse LES simulation. A zoomed-in view of the contours near the bottom left corner is provided as well.

Fig. 8. An instantaneous snapshot of the temperature from the pure RANS simulation. A zoomed-in view of the contours near the bottom left corner is provided as well.

5.2. Estimating the LES zone weight (σ^{L}) by comparing the turbulence lengthscales and the grid size

One of the main purposes of this study is to design a new criterion that determines σ^{L} by assessing the resolution of the LES grid and successfully use this criterion in a dual-mesh simulation of the square cavity flow. The basic idea behind a criterion of this type is that it gives $\sigma^{L} = 1$ at the locations where the LES is well-resolved and gives $\sigma^{L} = 0$ at the remaining locations. The development of this criterion was motivated by the complexity that is present in this flow as it features coexistence of laminar and turbulent zones. The Re_y criterion (see Equation (8)) gives $\sigma^{L} = 0$ in the laminar regions and thus cannot distinguish between the laminarization in these regions and the laminarization that occurs in the viscosity affected region. Details of this behaviour as well as the results obtained using the Re_y criterion are included in Appendix C.

Three important studies in which the LES resolution was assessed by comparing the grid size to the turbulence lengthscales are the studies of Xiao et al. (2014), Addad et al. (2008) and Uribe et al. (2010). Xiao et al. (2014) designed a criterion that assesses the grid resolution in the three different directions by defining a turbulence lengthscale associated with each direction and comparing it to the filter width in that direction. In this study, however, for simplicity we base our criterion on turbulence lengthscales that are scalar quantities rather than vectors or tensors. Addad et al. (2008) argued that the LES can be considered to be well-resolved at locations where the grid size (Δ) satisfies the following condition:

$$\Delta < \max\left(\lambda, \frac{L_{RM}}{10}\right) \tag{28}$$

where L_{RM} and λ are the RANS predictions of the integral and Taylor lengthscales, respectively:

$$L_{RM} = \frac{k^{3/2}}{\varepsilon} \tag{29}$$

$$\lambda = \sqrt{\frac{10\nu k}{\varepsilon}} \tag{30}$$

The lengthscale $\frac{L_{RM}}{10}$ was introduced as a lower limit in Equation (28) because for high Reynolds numbers, the grid size does not need to be as small as the Taylor lengthscale (λ) and the resolution can be considered adequate if the grid allows resolving eddies with lengthscales greater than one tenth of the integral lengthscale (Addad et al. (2008)).

In the study of Uribe et al. (2010), the authors formulated their RANS-LES blending functions as:

$$f_b = tanh\left(C_1 \frac{\varphi k^{3/2}}{\varepsilon \Delta}\right)^n \qquad (31)$$

where C_1 and n are constants. This function assesses the resolution of the LES grid by comparing the grid spacing Δ to the lengthscale $\frac{\varphi k^{3/2}}{\varepsilon}$ which represents the integral lengthscale $\frac{k^{3/2}}{\varepsilon}$ multiplied by the wall-normal anisotropy $\varphi = \frac{\langle v^2 \rangle}{k}$ (the ratio of the wall-normal Reynolds stress to the turbulent kinetic energy). Multiplying the integral lengthscale by φ provides a damping of the former in the near-wall region as $\frac{k^{3/2}}{\varepsilon}$ can become large in this region. A comparison of $\frac{k^{3/2}}{\varepsilon}$ and $\frac{\varphi k^{3/2}}{\varepsilon}$ in the near-wall region of a channel flow can be found in Uribe (2006).

In this study we first choose to combine the resolution criterions of Addad et al. (2008) and Uribe et al. (2010). This was done by starting from Equation (28) and multiplying both the integral and Taylor lengthscales by a damping function as:

$$\Delta < \max\left(\psi\lambda, \psi\frac{L_{RM}}{10}\right) \qquad (32)$$

where the damping function ψ was defined using the elliptic blending parameter α (see Appendix A) as follows:

$$\psi = \frac{3}{2}\left((1-\alpha^3)\varphi + \alpha^3 \frac{2}{3}\right) \qquad (33)$$

Using this function in Equation (32) damps the integral and Taylor lengthscales close to the wall since as the wall is approached the values of α and φ go to 0 and as a result the damping function ψ becomes approximately equal to $\frac{3}{2}\varphi$ which approaches 0. On the other hand, at locations far enough from the wall for α to become close to 1, ψ approaches 1 and thus the lengthscales λ and $\frac{L_{RM}}{10}$ in Equation (32) are not damped. ψ was not formulated using $\psi = \frac{3}{2}\varphi$ since far from the wall φ is not guaranteed to become equal to $\frac{2}{3}$ (meaning ψ can be smaller than 1 at large wall distances). For instance even in the centreline of a channel, turbulence is not isotropic (the three normal Reynolds stresses are not equal at this location) and thus φ does not equal $\frac{2}{3}$ (see for example the DNS data of Kawamura et al. (1998)).

In contrast to the flow studied here, the test cases in Xiao et al. (2014), Addad et al. (2008) and Uribe et al. (2010) do not feature unsteadiness, buoyancy forces or flow laminarization. Therefore, the new criterion has to be designed to account for these flow features. This gives the new criterion the advantage that it can be used for buoyancy driven flows, where the aforementioned features are quite often found.

One point worth noting is that the lengthscales λ and L_{RM} were calculated here using the total RANS turbulent kinetic energy (${k^R}_{Total}$) and the total RANS dissipation rate (${\varepsilon^R}_{Total}$) which were calculated from the pure RANS results as:

$$L_{RM} = \frac{{k^R}_{Total}^{3/2}}{{\varepsilon^R}_{Total}} \tag{34}$$

$$\lambda = \sqrt{\frac{10\nu {k^R}_{Total}}{{\varepsilon^R}_{Total}}} \tag{35}$$

where ${k^R}_{Total}$ and ${\varepsilon^R}_{Total}$ were calculated as:

$${k^R}_{Total} = \{k^R\} + {k^R}_{Res} \tag{36}$$

$${\varepsilon^R}_{Total} = \{\varepsilon^R\} + {\varepsilon^R}_{Res} \tag{37}$$

where {} is used here to represent quantities averaged in time using a simple arithmetic mean operation. k^R and ${k^R}_{Res}$ are the pure RANS modelled and resolved turbulent kinetic energies[2], respectively. ${k^R}_{Res}$ was calculated as:

$${k^R}_{Res} = 0.5 * \left\{{u_i''}^R\, {u_i''}^R\right\} \tag{38}$$

where ${u_i''}^R = \langle U_i \rangle - \{\langle U_i \rangle\}$ represents the resolved RANS velocity fluctuation. In addition, ε^R and ${\varepsilon^R}_{Res}$ are the pure RANS modelled and resolved turbulent dissipation rates[3], respectively. ${\varepsilon^R}_{Res}$ was estimated using:

$${\varepsilon^R}_{Res} = 2\nu\left\{\langle S_{ij}\rangle\langle S_{ij}\rangle\right\} \tag{39}$$

$$\langle S_{ij}\rangle = 0.5\left(\frac{\partial\langle U_i\rangle}{\partial x_j} + \frac{\partial\langle U_j\rangle}{\partial x_i}\right) \tag{40}$$

The problem with Equation (32) is that in laminar zones it is difficult to predict the behaviour of the lengthscales L_{RM} and λ. The definitions in Equations (34) and (35) are not guaranteed to give lengthscales that are greater than 0 in all the laminar zones. If L_{RM} and λ both become equal to 0 at a particular location, Equation (32) will see that the grid size is greater than the turbulence lengthscales, which is a false indication of an under-resolved LES at this location. As a result, in the dual-mesh context the LES will be forced towards the RANS at this location. This can be problematic at the laminar locations where instabilities that enhance the turbulence levels form (in this cavity flow these instabilities exist near the top right and bottom left corners). Forcing the LES fluctuations at these locations can destroy the LES instabilities and affect the predicted turbulence levels. In addition, one would

---

[2] *What is meant here by the RANS resolved turbulent kinetic energy is the kinetic energy of the unsteady motions resolved in the RANS simulation which represent mean flow instabilities rather than turbulence.*

[3] *The RANS resolved turbulent dissipation rate term was used to represent the rate at which the energy of the unstable motions resolved in the RANS simulation is dissipated into heat.*

want the LES to drive the RANS at all the laminar locations as the LES does a better job than the RANS in predicting the interaction of the laminar zones with the turbulent ones.

To prevent the condition in Equation (32) from being violated in the laminar zones, the lengthscales were limited by making use of the pure RANS prediction of the Kolmogorov lengthscale (η) as:

$$\Delta < \max\left(\psi\lambda, \psi\frac{L_{RM}}{10}, 8C_{kolm}\eta\right) \qquad (41)$$

where:

$$\eta = \left(\frac{\nu^3}{\{\varepsilon^R\}}\right)^{\frac{1}{4}}, \qquad (42)$$

$$C_{kolm} = \begin{cases} 1 & for\ \mathrm{d} \geq \Delta_{max}, \\ 0.3125 & for\ \mathrm{d} < \Delta_{max} \end{cases} \qquad (43)$$

where d is the wall distance and $\Delta_{max} = \max(\Delta_x, \Delta_y, \Delta_z)$ is the largest cell size in the three directions.

It can be observed that the time average of the RANS modelled dissipation rate ($\{\varepsilon^R\}$) is used in the definition of the Kolmogorov lengthscale and not the total dissipation rate ${\varepsilon^R}_{Total}$ (${\varepsilon^R}_{Total}$ was used in the definitions of the integral and Taylor scales). This is to make the product 8 η much larger than the grid size Δ in the laminar zones where $\varepsilon^R \to 0$. This in turn allows the criterion in Equation (41) to correctly predict that the LES is well-resolved at the laminar zones. 8η is multiplied by C_{kolm} in order to provide a damping in the viscous sublayer as 8 η becomes much larger than $\psi\lambda$ and $\psi\frac{L_{RM}}{10}$ and might become larger than the grid size in this region. This damping thus prevents the quantity $8C_{kolm}\eta$ from becoming larger than the grid size in the viscosity affected region (otherwise the criterion might falsely indicate that the LES is well-resolved at some locations in the sublayer).

In Equation (43), it is assumed that wall distances lower than the value of Δ_{max} correspond to the viscous sublayer. The justification for this assumption is that the purpose of damping the Kolmogorov lengthscale using C_{kolm} is to prevent the maximum lengthscale in Equation (41) from becoming larger than the grid size near the wall for coarse LES grids. For these grids, a wall distance equal to the maximum grid spacing Δ_{max} corresponds to a y^+ that is definitely greater than 11. Thus, the Kolmogorov damping we introduced remains active over the entire viscous sublayer (the viscosity affected region extends up to a y^+ of about 11). The criterion in Equation (41) can be used to estimate the LES zone weight (σ^L) in the hybrid simulation using:

$$\sigma^L = \begin{cases} 1 & for\ \Delta < \max\left(\psi\lambda, \psi\frac{L_{RM}}{10}, 8C_{kolm}\eta\right) \\ 0 & for\ \Delta > \max\left(\psi\lambda, \psi\frac{L_{RM}}{10}, 8C_{kolm}\eta\right) \end{cases} \qquad (44)$$

One observation that can be made about this equation is that σ^L does not need to be calculated repeatedly during the entire dual-mesh hybrid simulation. This is because all the turbulence lengthscales in Equation (44) are calculated from the pure RANS results. The use of hybrid RANS to estimate these lengthscales was avoided as the relaxation forcing in the LES regions can pollute predictions of the turbulence quantities in these regions. Therefore, one can run the pure RANS simulation, calculate the required lengthscales and then run the dual-mesh simulation (it is a good practice to run the pure RANS before the dual-mesh simulation since the pure RANS results give good initial conditions for the hybrid RANS simulation). σ^L can then be calculated at one of the initial time steps of the dual-mesh simulation since nothing in Equation (44) changes during this simulation. In order to calculate σ^L in the hybrid simulation, the turbulence lengthscales in Equation (44) need to be interpolated into the LES grid so that they can be compared to Δ, which we chose to calculate as the cubic root of the volume of the cell[4] $\left(\Delta_x \Delta_y \Delta_z\right)^{1/3}$. After this σ^L can be interpolated into the RANS grid so that it can be used in the RANS equations.

In Fig. 9, a contour plot of σ^L from a hybrid simulation in which it was estimated using the new lengthscale criterion is presented. It can be seen that Equation (44) gives the required behaviour of σ^L. σ^L is equal to 1 in the laminar core and the regions where σ^L is equal to 0 (RANS regions) near the top right and bottom left corners are very thin. Profiles of σ^L near the hot wall are also shown in Fig. 10.

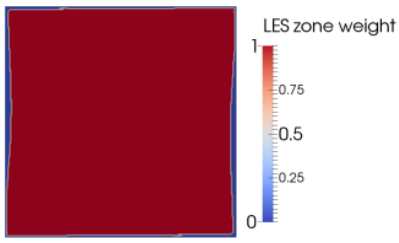

Fig. 9. Contours of the LES zone weight (σ^L) from a hybrid simulation in which it was estimated using Equation (44).

[4] *Δ was not calculated as $max(\Delta_x, \Delta_y, \Delta_z)$ in order to avoid ending up with thick RANS regions (with $\sigma^L = 0$) close to the horizontal walls.*

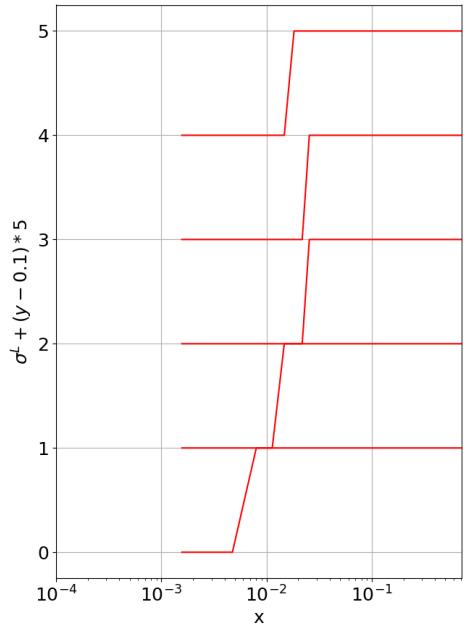

Fig. 10. Mean values of the LES zone weight (σ^{L}) from a hybrid simulation in which it was calculated using Equation (44). This figure shows σ^{L} profiles at horizontal lines that correspond to cavity heights equal to $0.1H$, $0.3H$, $0.5H$, $0.7H$ and $0.9H$. The horizontal axis is in log scale.

Plots of the lengthscales $\psi\lambda$, $\psi\frac{L_{RM}}{10}$,$8C_{kolm}\eta$, 8η and Δ at four cavity heights are shown in Fig. 11 (a)-(d). The damping of the integral and the Taylor lengthscales that is introduced by the function ψ results in a relatively smooth change of these lengthscales with the wall distance in the wall vicinity compared to the behaviour of the undamped lengthscales λ, $\frac{L_{RM}}{10}$ which can be seen in Fig. 12. The undamped lengthscales can also be observed to become quite large close to the wall.

It can be seen from Fig. 11 that close to the wall, the quantity 8η becomes much larger than the lengthscales $\psi\lambda$ and $\psi\frac{L_{RM}}{10}$. On the other hand, the quantity $8C_{kolm}\eta$ which equals 2.5 η at wall distances less than Δ_{max} (see Equation (43)) appears to provide a much more reasonable estimation of the near-wall turbulence lengthscale than 8η. $8C_{kolm}\eta$ can be observed to become quite large at $x = 0.1$ (which corresponds to an average x^{+} of around 885). This is because of the almost vanishing turbulence at this location (see the pure RANS turbulent kinetic energy profiles in Fig. 4 (b)) which causes a small value of ε^{R} which leads to a large estimation of $8C_{kolm}\eta$ (see the definition of η in Equation (42)).

Fig. 11 shows that $\psi\frac{L_{RM}}{10}$ and $\psi\lambda$ are not close to 0 at $x = 0.1$. This is because these two lengthscales have been based on the RANS total turbulent kinetic energy (${k^{R}}_{Total}$) and the RANS total dissipation rate (${\varepsilon^{R}}_{Total}$). These

two quantities do not approach 0 at $x = 0.1$. Even though at this location the turbulent fluctuations are very weak (meaning both k^R and ε^R approach 0), the unsteady motion of the core makes ${k^R}_{Res}$ and ${\varepsilon^R}_{Res}$ non-zero resulting in nonzero values of ${k^R}_{Total}$ and ${\varepsilon^R}_{Total}$. The large values of $\psi\frac{L_{RM}}{10}$ and $\psi\lambda$ serve to prevent σ^L from falling to zero, and hence prevent the RANS from driving the LES outside the boundary layer.

As mentioned previously, the lengthscale $8C_{kolm}\eta$ is used in Equation (44) to provide an additional safeguard that prevents the condition in the equation from being violated in laminar zones, where the lengthscales $\psi\frac{L_{RM}}{10}$ and $\psi\lambda$ are not guaranteed to become large. In Fig. 11 (e), a plot of the turbulence lengthscales at a vertical line located at a horizontal distance of $0.1H$ from the hot wall is shown. This location features low turbulence levels but is dominated by the unsteady motions which have been discussed previously. The low turbulence levels at this location result in a low ε^R and make $8C_{kolm}\eta$ larger than the other lengthscales ($\psi\frac{L_{RM}}{10}$ and $\psi\lambda$) up to a wall distance of about $0.01H$. This relatively high near-wall value of $8C_{kolm}\eta$ makes σ^L rise to 1 at a distance of about 0.008 from the wall as a consequence of Δ becoming less than $8C_{kolm}\eta$ at this wall distance (Fig. 13).

If one was relying only on the lengthscales $\psi\frac{L_{RM}}{10}$ and $\psi\lambda$, the distance at which σ^L becomes 1 would have been larger than 0.008. This can be observed from Fig. 11 (e) which shows that the wall distance after which Δ becomes smaller than the lengthscales $\psi\frac{L_{RM}}{10}$ and $\psi\lambda$ is larger than the distance where Δ starts becoming smaller than the lengthscale $8C_{kolm}\eta$. It is better to minimize the wall distance at which σ^L becomes 1 near the top right and bottom left corners in order to avoid the risk of damping the instabilities present in the hybrid LES simulation at these locations. Introducing the lengthscale $8C_{kolm}\eta$ as an argument in Equation (44) thus serves as a shield against a late RANS-LES switch near the top right and bottom left corners. However, one still needs to avoid having a large grid size Δ near these corners as this can result in a delay of the RANS-LES switch.

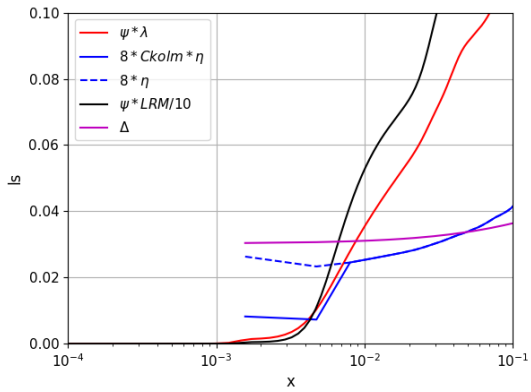

(a)

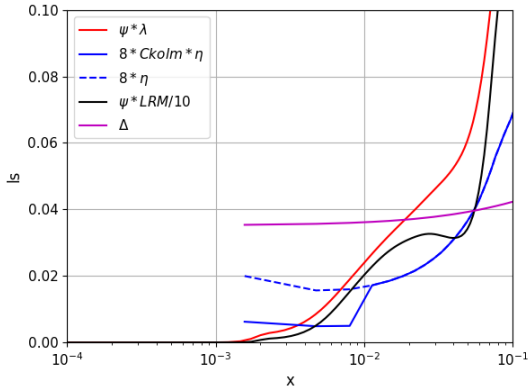

(b)

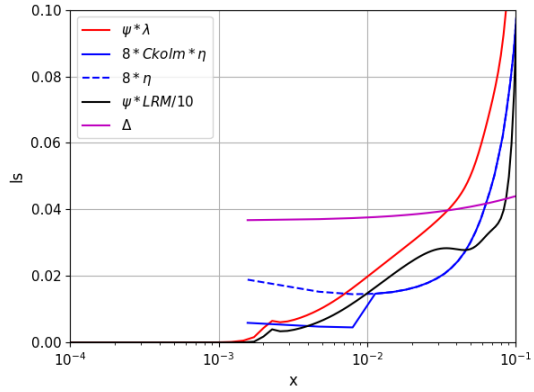

(c)

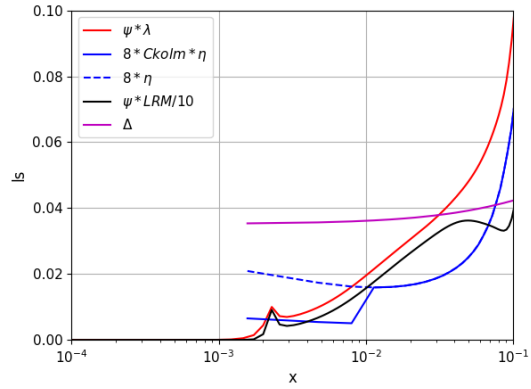

(d)

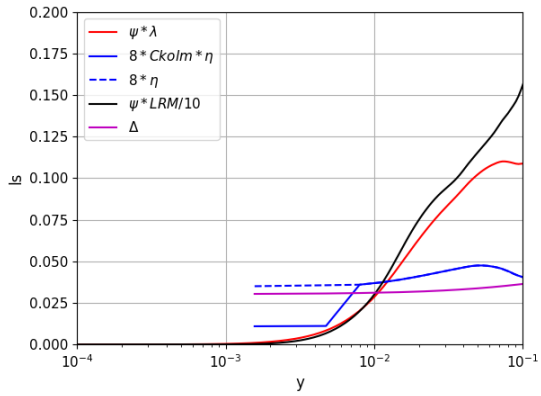

(e)

Fig. 11. Plots of the lengthscales $\psi\lambda$, $\psi\frac{L_{RM}}{10}$, 8η and $8C_{kolm}\eta$ as well as the filter width Δ (calculated as the cubic root of the volume of the cell) at horizontal lines that correspond to cavity heights equal to (a) $0.1H$ (b) $0.3H$ (c) $0.5H$ (d) $0.7H$. The profiles of the lengthscales and the filter width shown in (e) are at a vertical line that is located at a distance of $0.1H$ from the hot wall. The horizontal axis is in log scale.

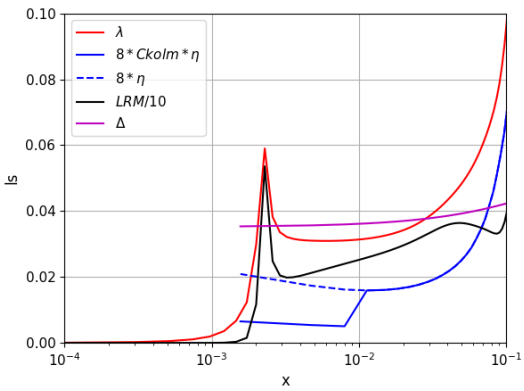

Fig. 12. A plot of the lengthscales λ, $\frac{L_{RM}}{10}$, 8η and $8C_{kolm}\eta$ as well as the filter width Δ (calculated as the cubic root of the volume of the cell) at a horizontal line that corresponds to the cavity height equal to $0.7H$. The horizontal axis is in log scale.

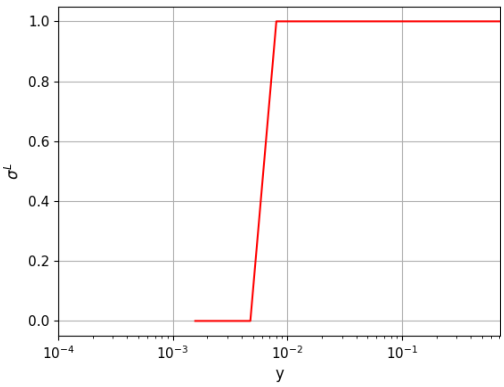

Fig. 13. A plot of the LES zone weight (σ^L) at a vertical line that is located at a distance of $0.1H$ from the hot wall. This plot is from a hybrid simulation in which σ^L was estimated using Equation (44). The horizontal axis is in log scale.

5.3. Dual-mesh results obtained using the new resolution criterion

The fact that the regions in which σ^L is 0 near the top right and bottom left corners are thin causes the hybrid RANS instability to be almost eliminated (see Fig. 15). The reason why the hybrid RANS becomes steady is the vigorous forcing of the RANS towards the LES in these regions. The averaged LES field is steady (the chosen EWA averaging period is large enough to smooth the LES field) and forcing the RANS towards it in a significant part of the region where the RANS instability forms eliminates the unsteadiness.

The fact that the hybrid RANS becomes steady simplifies the application of the dual-mesh approach as one does not need to take into account the time dependency of the RANS simulation when coupling the RANS and the LES.

In this case, the only requirement that has to be satisfied by T_{avg} is that it has to be large enough to smooth the LES quantities and remove all the fluctuations. Although not shown here, the fact that the results of this section hardly changed when the averaging time scale was doubled suggests that $T_{avg} = 32\,\frac{H}{\sqrt{g\beta H\Delta T}}$ is large enough to smooth out the turbulence structures.

The hybrid simulations perform well in predicting the vertical velocities near the hot wall as shown Fig. 16 (a). This is because the hybrid RANS-LES coupling does not damp the instability in the hybrid LES simulation as can be seen from the snapshot of the hybrid LES temperature field shown in Fig. 14. The reason why the LES instability is not damped is that at the locations where the LES instability is dominant (near the top right and bottom left corners), the LES is forced towards the RANS in only a thin layer close to the wall. Capturing this instability allows the LES to predict the high turbulence levels along the vertical walls as these high levels are triggered by the flow unsteadiness.

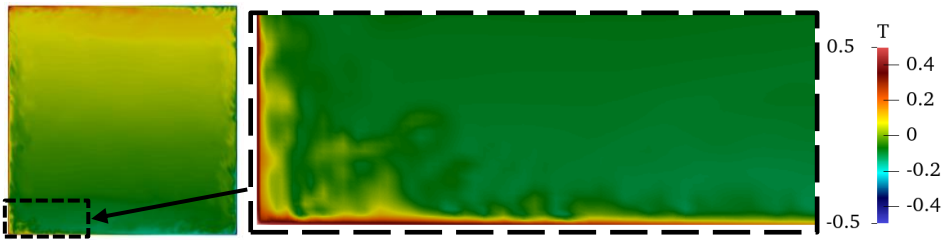

Fig. 14. An instantaneous snapshot of the LES temperature from a hybrid simulation in which the LES zone weight was calculated using Equation (44). A zoomed-in view of the contours near the bottom left corner is provided as well.

Fig. 15. An instantaneous snapshot of the RANS temperature from a hybrid simulation in which the LES zone weight was calculated using Equation (44). A zoomed-in view of the contours near the bottom left corner is provided as well.

The predictions of the total turbulent kinetic energy profiles of the flow near the hot wall are shown in Fig. 16 (b). The reasonable hybrid predictions of these profiles at the downstream locations of the boundary layer are a

consequence of not damping the plume instability in the hybrid LES simulation. However, admittedly the hybrid method's predictions of the TTKE profiles worsen as the bottom wall is approached due to the low turbulence levels in the upstream region of the hot wall's boundary layer. The significant underprediction of the TTKE at the height of $0.1H$ is consistent with the poor hybrid velocity predictions at the same location. Fig. 17 also shows that the temperature profiles are of reasonable accuracy at all the locations apart from the height of $0.1H$.

It can be observed from Fig. 16 (a) that the hybrid LES simulation does a good job in capturing the interaction of the turbulent boundary layer with the laminar core. Note that the coarseness of the LES grid only allows capturing the outer edge of the boundary layer, since only the first and second cells contain the peak of the velocity profile, and the wall-jet side is fairly well modelled with the hybrid RANS. Conversely, the pure RANS simulation performed rather poorly on the cavity side but the RANS is aptly corrected by the LES when run in a hybrid simulation (the continuous red line is almost overlapped by the DNS symbols at most of the locations).

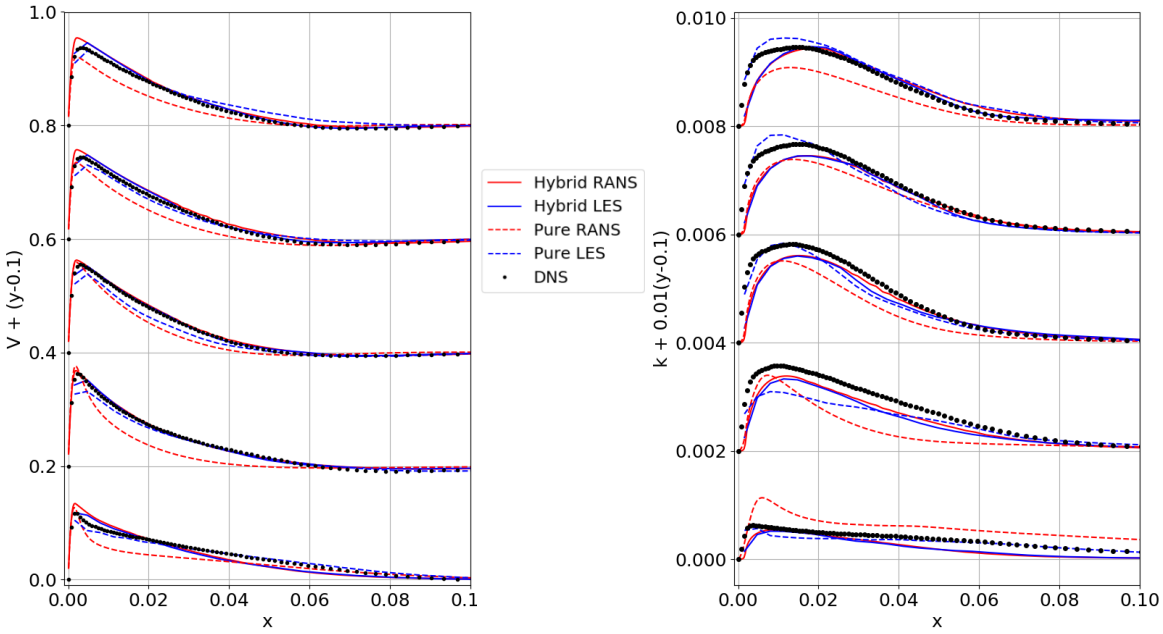

(a) (b)

Fig. 16. Plots showing the pure RANS, pure LES, hybrid RANS and hybrid LES predictions of the profiles of the mean vertical velocity (shown in (a)) and the total turbulent kinetic energy (shown in (b)) near the hot wall at horizontal lines that correspond to cavity heights equal to $0.1H$, $0.3H$, $0.5H$, $0.7H$ and $0.9H$. In the hybrid simulations σ^L was calculated using Equation (44).

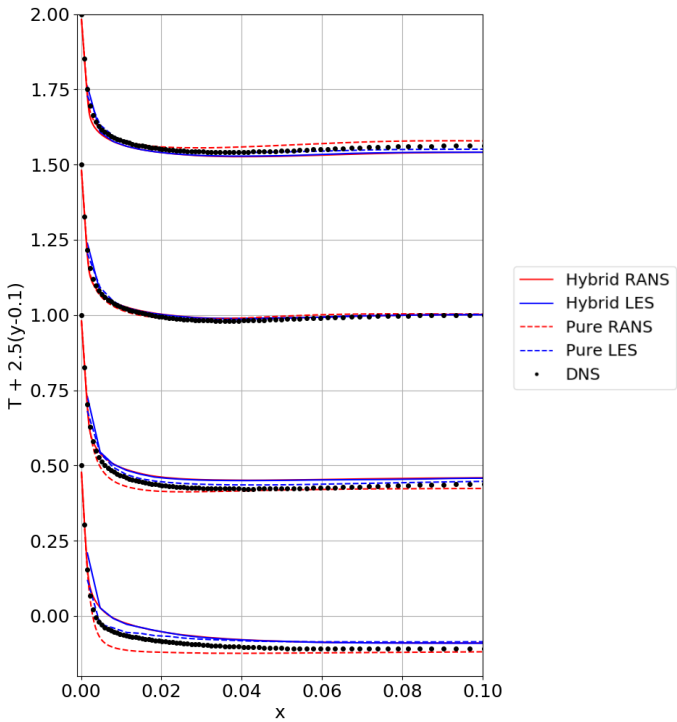

Fig. 17. A plot showing the pure RANS, pure LES, hybrid RANS and hybrid LES predictions of the mean temperature profiles near the hot wall at horizontal lines that correspond to cavity heights equal to $0.1H$, $0.3H$, $0.5H$ and $0.7H$. In the hybrid simulations σ^L was calculated using Equation (44).

The horizontal velocity profiles at the midwidth obtained using the different simulations are shown in Fig. 18. It can be seen from this figure that the hybrid simulations and the pure coarse LES do a much better job in predicting the velocity profile than the pure RANS. This is because the pure RANS performs worse than the other simulations in predicting the velocities at the hot wall boundary layer (Fig. 16 (a)).

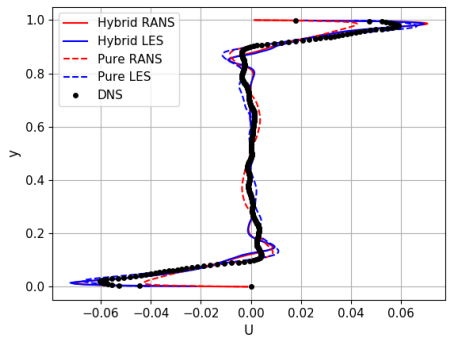

Fig. 18. A plot showing the pure RANS, pure LES, hybrid RANS and hybrid LES predictions of the mean horizontal velocity at the cavity midwidth. In the hybrid simulations σ^L was calculated using Equation (44).

The wall shear stress (WSS) profiles along the hot wall are shown in Fig. 19 (a). It can be seen that the hybrid LES does not accurately predict the WSS. This is because even though the EWA velocities at the near-wall nodes of the LES are forced towards the corresponding RANS velocities, the wall distances of these nodes are large enough to make the error associated with the finite difference approximation of the velocity gradient at the wall non-negligible. This is the reason why the inaccuracy of the hybrid LES WSS is inevitable and one should consider the hybrid RANS WSS predictions instead. In fact, the hybrid RANS gives reasonable predictions of the WSS apart from a small overprediction between $y = 0.4$ and $y = 1$ which is caused by an overprediction of the velocity peaks at these heights. This overprediction can be seen in the velocity profiles at the heights of $0.5H$, $0.7H$ and $0.9H$ (Fig. 16 (a)). On the other hand, the pure RANS slightly overestimates the WSS at the bottom half of the hot wall which is consistent with the overprediction of the velocity in the immediate wall vicinity which can be clearly seen in Fig. 16 (a).

As regards the Nusselt number (Nu) predictions shown in Fig. 19 (b), the hybrid RANS does not seem to be superior to the pure LES. However, one can observe that the hybrid RANS seems to give a more accurate prediction of the locations of the local minima and local maxima of the Nu profile (between about $y = 0.2$ and 0.4) in comparison to the pure coarse LES and pure RANS simulations. The local maxima and minima of the Nu are related to a turbulence enhancement that occurs along the hot wall (Sebilleau (2016)). The fact that the locations of these points are captured with the hybrid method suggests that the method is able to accurately predict the location of the turbulence enhancement. The underprediction of the Nu by the hybrid RANS seems to be because the RANS closure is incapable of accurately predicting the Nu in this flow. Future studies should focus on studying the impact of using different RANS models and different turbulent heat flux treatments on the predicted Nusselt number profile.

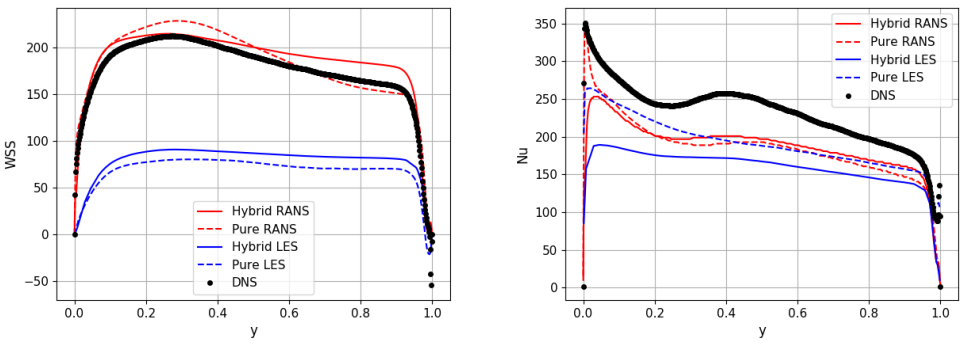

(a) (b)

Fig. 19. Predictions of the wall shear stress (shown in (a)) and the Nusselt number (shown in (b)) along the hot wall of the pure RANS, pure LES, hybrid RANS and hybrid LES simulations. In the hybrid simulations σ^L was calculated using Equation (44).

The temperature variance predictions are presented in Fig. 20. It can be seen that at the heights of $0.3H$, $0.5H$, $0.7H$ and $0.9H$, the hybrid RANS and hybrid LES are superior to the pure coarse LES in predicting the temperature variance at locations to the right of the peaks of the variance. This is because forcing the LES towards the RANS close to the wall solves the problem of overpredicting the variance that is present in the pure coarse LES results. However, the peaks of the temperature variance are underestimated by the hybrid simulations at all the cavity heights. Again, the problem here lies in the RANS closure, which is unable to accurately predict the temperature fluctuations in the immediate near-wall region.

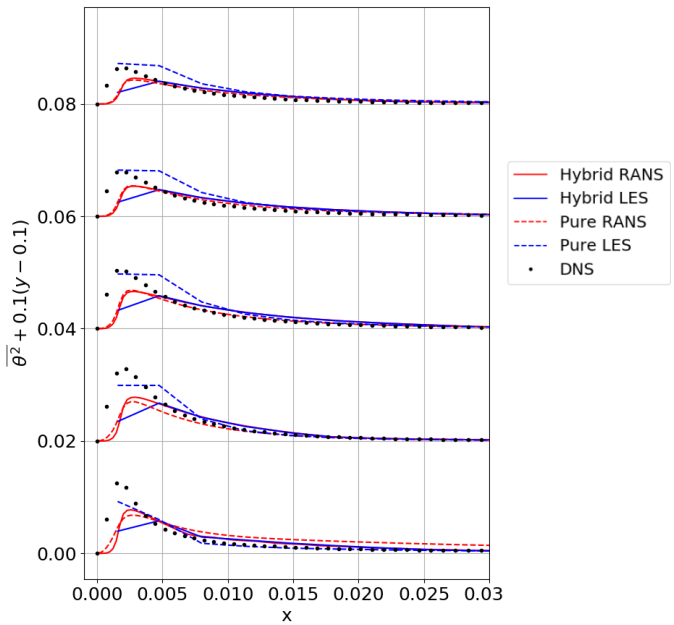

Fig. 20. A plot showing the pure RANS, pure LES, hybrid RANS and hybrid LES predictions of the temperature variance profiles near the hot wall at horizontal lines that correspond to cavity heights equal to $0.1H$, $0.3H$, $0.5H$, $0.7H$ and $0.9H$. In the hybrid simulations σ^L was calculated using Equation (44).

6. Conclusions

In this study, the performance of different turbulence modelling approaches in predicting a high Rayleigh number buoyant square cavity flow was assessed. This flow features boundary layers with a relatively small thickness (due to the high Ra) , a laminar stably stratified core and unstably stratified regions near the downstream halfs of the horizontal walls. The latter causes the presence of an instability in this flow that enhances the turbulence levels. The simulations that were run included a pure unsteady RANS, a pure coarse LES as well as dual-mesh hybrid RANS-LES simulations.

The RANS was found to perform poorly in capturing the flow in the later stages of the boundary layer. Contrarily, the coarse LES was found to be superior to the RANS in capturing the outer edge of the boundary layer. The main problem with the pure coarse LES is that it is unable to predict the near-wall part of the boundary layer. The reasons for this are mainly that the coarse LES does not capture the structures in the viscosity affected region and that the near-wall nodes are located at a distance large enough to prevent an accurate estimation of the near-wall gradients. In addition, an overestimation of the temperature fluctuations in the coarse LES results was observed.

It has been found that in order to successfully compute this flow with the dual-mesh approach, the σ^L determining criterion has to be able to distinguish the laminar zones in this flow from the viscosity affected near-wall regions of the turbulent zones. Consequently, a new criterion that can be considered to belong to the family of criterions

based on comparing the turbulence lengthscales and the grid size was developed and analysed here. This criterion was designed in a way that makes it suitable for natural convection flows featuring laminar regions that coexist with other regions that are turbulent. This criterion also has the advantages of the criterions of both Addad et al. (2008) and Uribe et al. (2010) and can be used when computing non-buoyant flows. For these flows, however, there is no need to include the lengthscale $8C_{kolm}\eta$ in Equation (44).

The dual-mesh results yielded by the new lengthscale criterion for the square cavity flow were found to be of reasonable accuracy. Future dual-mesh studies of the square cavity should focus on finding which RANS closures can provide accurate estimations of the Nusselt number and the temperature variance in the immediate wall vicinity. A subsequent paper will show that the new lengthscale criterion performs satisfactorily in determining the RANS and the LES regions in a buoyant flow in a cylindrical annuli. These cylindrical annuli results can also be found in the PhD thesis of the first author (Ali (2020)) and in Revell et al. (2020).

Acknowledgements

The authors would like to thank Siemens in particular Sylvain Lardeau for funding this work. The authors are also grateful to Ryan Tunstall for providing his dual-mesh code. The authors would also like to thank the UK Department of Business, Energy and Industrial Strategy (BEIS) for the financial support through Newton institutional links fund (Engineering Sustainable Solar Energy and Thermocline Alternatives-ESSEnTiAl, Grant ID 332271136). The authors are also thankful to Frederic Sebilleau for providing the DNS data.

References

Abed, N., & Afgan, I. (2017). A CFD study of flow quantities and heat transfer by changing a vertical to diameter ratio and horizontal to diameter ratio in inline tube banks using URANS turbulence models. International Communications in Heat and Mass Transfer, 89, 18-30.

Abed, N., Afgan, I., Iacovides, H., Cioncolini, A., & Nasser, A. (2020a). Assessment and Evaluation of the Thermal Performance of Various Working Fluids in Parabolic trough Collectors of Solar Thermal Power Plants under Non-Uniform Heat Flux Distribution Conditions. Energies, 13 (15), 3776. https://doi.org/10.3390/en13153776

Abed, N., Afgan, I., Cioncolini, A., Nasser, A., & Mekhail, T. (2020b). Thermal performance evaluation of various nanofluids with non-uniform heating for parabolic trough collectors. Case Studies in Thermal Engineering, 22, 100769.

Abed, N., & Afgan, I. (2020). An extensive review of various technologies for enhancing the thermal and optical performances of parabolic trough collectors. International Journal of Energy Research. 2020, 44 (7), 5117-

5164. https://doi.org/10.1002/er.5271

Abramov, A. G., & Smirnov, E. M. (2006). Numerical simulation of turbulent convection of air in a square cavity heated on the side. High Temperature, 44(1), 91–98.

Addad, Y., Gaitonde, U., Laurence, D., & Rolfo, S. (2010). Optimal Unstructured Meshing for Large Eddy Simulations. Quality and Reliability of Large-Eddy Simulations. https://link.springer.com/content/pdf/10.1007%2F978-1-4020-8578-9.pdf

Afgan, I., Moulinec, C., & Laurence, D. (2008). Numerical simulation of generic side mirror of a car using large eddy simulation with polyhedral meshes. International journal for numerical methods in fluids, 56 (8), 1107-1113.

Ahmed, U., Apsley, D., Stallard, T., Stansby, P., & Afgan, I. (2020). Turbulent length scales and budgets of Reynolds stress-transport for open-channel flows; friction Reynolds numbers (Reτ) = 150, 400 and 1020. Journal of Hydraulic Research, pp 1-15.

Ali, A.E.A. (2020). Dual-mesh hybrid RANS-LES computations of turbulent natural convection flows. University of Manchester.

Ammour, D., Craft, T., & Iacovides, H. (2013). Highly resolved les and URANS of turbulent buoyancy-driven flow within inclined differentially-heated enclosures. Flow, Turbulence and Combustion, 91(3), 669–696. https://doi.org/10.1007/s10494-013-9497-1

Ampofo, F., & Karayiannis, T. G. (2003). Experimental benchmark data for turbulent natural convection in an air filled square cavity. International Journal of Heat and Mass Transfer, 46(19), 3551–3572. https://doi.org/10.1016/S0017-9310(03)00147-9

Barhaghi, D. G. G., & Davidson, L. (2007). Natural convection boundary layer in a 5:1 cavity. Physics of Fluids, 19(12), 1–15. https://doi.org/10.1063/1.2815746

Benhamadouche, S., Afgan, I., & Manceau, R. (2020). Numerical Simulations of Flow and Heat Transfer in a Wall-Bounded Pin Matrix. Flow Turbulence and Combustion, 104 (1), 19-44.

Betts, P. L., & Bokhari, I. H. (2000). Experiments on turbulent natural convection in an enclosed tall cavity. International Journal of Heat and Fluid Flow, 21(6), 675–683. https://doi.org/10.1016/S0142-727X(00)00033-3

Billard, F., & Laurence, D. (2012). A robust k − ε − v 2/k elliptic blending turbulence model applied to near-wall, separated and buoyant flows. International Journal of Heat and Fluid Flow, 33(1), 45–58.

Craft, T. J., Gerasimov, A. V., Iacovides, H., & Launder, B. E. (2002). Progress in the generalization of wall-function treatments. International Journal of Heat and Fluid Flow, 23(2), 148–160.

https://doi.org/10.1016/S0142-727X(01)00143-6

Davidson, L. (2019). Non-zonal detached eddy simulation coupled with a steady RANS solver in the wall region. ERCOFTAC Bullentin 89, Special Issue on Current trends in RANS-based scale-resolving simulation methods.

de Laage de Meux, B., Audebert, B., Manceau, R., & Perrin, R. (2015). Anisotropic linear forcing for synthetic turbulence generation in large eddy simulation and hybrid RANS/LES modeling. Physics of Fluids, 27. https://doi.org/10.1063/1.4916019

Durbin, P. A. (1991). Near-wall turbulence closure modeling without "damping functions." Theoretical and Computational Fluid Dynamics, 3(1), 1–13. https://doi.org/10.1007/BF00271513

Fureby, C., Tabor, G., Weller, H. G., Gosman, A. D., & Tabor,) G. (1997). A comparative study of subgrid scale models in homogeneous isotropic turbulence. Physics of Fluids Physics of Fluids A: Fluid Dynamics, 9(4), 1416–1492. https://doi.org/10.1063/1.858423

Guleren, K. M., Afgan, I., & Turan, A. (2010). Predictions of turbulent flow for the impeller of a NASA low-speed centrifugal compressor. Journal of Turbomachinery-Transactions of the ASME, 132 (2)-21005.

Han, X., Sagaut, P., Lucor, D., & Afgan, I. (2012). Stochastic response of the laminar flow past a flat plate under uncertain inflow conditions. International Journal of Computational Fluid Dynamics, 26 (2), 101-117.

Hanjalić, K., Popovac, M., & Hadžiabdić, M. (2004). A robust near-wall elliptic-relaxation eddy-viscosity turbulence model for CFD. International Journal of Heat and Fluid Flow, 25(6), 1047–1051. https://doi.org/10.1016/j.ijheatfluidflow.2004.07.005

Issa, R. I. (1986). Solution of the implicitly discretised fluid flow equations by operator-splitting. Journal of Computational Physics, 62(1), 40–65. https://doi.org/10.1016/0021-9991(86)90099-9

Kahil, Y., Benhamadouche, S., Berrouk, A. S., & Afgan, I. (2019). Simulation of subcritical-Reynolds-number flow around four cylinders in square arrangement configuration using LES. European Journal of Mechanics - B/Fluids, 74, 111-122.

Kawamura, H., Ohsaka, K., Abe, H., & Yamamoto, K. (1998). DNS of turbulent heat transfer in channel flow with low to medium-high Prandtl number fluid. International Journal of Heat and Fluid Flow, 19(5), 482–491. https://doi.org/10.1016/S0142-727X(98)10026-7

Kocutar, P., Škerget, L., & Ravnik, J. (2015). Hybrid LES/URANS simulation of turbulent natural convection by BEM. Engineering Analysis with Boundary Elements, 61, 16–26.

Kumar, R., & Dewan, A. (2016). A study of LES-SGS closure models applied to a square buoyant cavity. International Journal of Heat and Mass Transfer, 98, 164–175.

https://doi.org/10.1016/j.ijheatmasstransfer.2016.02.057

Manceau, R., Carpy, S., & Alfano, D. (2002). A RESCALED Î½2Â¯â^'f MODEL: FIRST APPLICATION TO SEPARATED AND IMPINGING FLOWS. Engineering Turbulence Modelling and Experiments 5: Proceedings of the 5th International Symposium on Engineering Turbulence Modelling and Measurements Mallorca, Spain, 16â€"18 September, 2002, 107–116. https://doi.org/10.1016/B978-008044114-6/50009-0

Manceau, R., & Hanjalić, K. (2002). Elliptic blending model: A new near-wall Reynolds stress turbulence closure. Physics of Fluids, 14(2), 744–754. https://doi.org/10.1063/1.1432693

Nguyen, P. T. L., Uribe, J .C., Afgan, Imran, & Laurence, D. R. (2020). A Dual-Grid Hybrid RANS/LES Model for Under-Resolved Near-Wall Regions and its Application to Heated and Separating Flows. Flow, Turbulence and Combustion, 104, 835–859.

Omranian, A., Craft, T. J., & Iacovides, H. (2014). The computation of buoyant flows in differentially heated inclined cavities. International Journal of Heat and Mass Transfer, 77, 1–16. https://doi.org/10.1016/j.ijheatmasstransfer.2014.04.068

Peng, S. H., & Davidson, L. (2001). Large eddy simulation for turbulent buoyant flow in a confined cavity. International Journal of Heat and Fluid Flow, 22(3), 323–331. https://doi.org/10.1016/S0142-727X(01)00095-9

Puragliesi, R., & Leriche, E. (2012). Proper orthogonal decomposition of a fully confined cubical differentially heated cavity flow at Rayleigh number Ra=109. Computers and Fluids, 61, 14–20. https://doi.org/10.1016/j.compfluid.2011.06.005

Revell, A., Afgan, I., Ali, A., Santasmasas, M., Craft, T., de Rosis, A., Holgate, J., Laurence, D., Iyamabo, B., Mole, A., Owen, B., Savoie, M., Skillen, A., Wang, J., & Zhang, X. (2020). Coupled Hybrid RANS-LES Research at the University of Manchester. ERCOFTAC Bulletin. 2020. Vol 120, Pages 67.

Sebilleau, F. (2016). Computational Analysis of Buoyancy driven flows across scales. Imperial College of Science, Technology and Medicine.

Sebilleau, Frederic, Issaa, R., Lardeau, S., & Walker, S. (2018). Direct Numerical Simulation of an air-filled differentially heated square cavity with Rayleigh numbers up to 1011. International Journal of Heat and Mass Transfer, 123, 297–319.

Tunstall, R. (2016). CFD and turbulence modelling for Nuclear Plant Thermal hydraulics systems. University of Manchester.

Tunstall, R., Laurence, D., Prosser, R., & Skillen, A. (2017). Towards a generalised dual-mesh hybrid LES/RANS framework with improved consistency. Computers and Fluids, 157, 73–83.

https://doi.org/10.1016/j.compfluid.2017.08.002

Uribe, J. . C., Jarrin, N., Prosser, R., & Laurence, D. (2010). Development of a Two-velocities Hybrid RANS-LES Model and its Application to a Trailing Edge Flow. Flow Turbulence and Combustion, 85, 181–197. https://doi.org/https://doi.org/10.1007/s10494-010-9263-6

Uribe, J. C. (2006). An industrial approach to near-wall turbulence modelling for unstructured nite volume methods. The University of Manchester.

van Leer, B. (1974). Towards the ultimate conservative difference scheme. II. Monotonicity and conservation combined in a second-order scheme. Journal of Computational Physics, 14(4), 361–370. https://doi.org/10.1016/0021-9991(74)90019-9

Wu, Z., Laurence, D., Iacovides, H., & Afgan, I. (2017a). Direct simulation of conjugate heat transfer of jet in channel crossflow. International Journal of Heat and Mass Transfer, 110, 193-208.

Wu, Z., Laurence, D., & Afgan, I. (2017b). Direct numerical simulation of a low momentum round jet in channel crossflow. Nuclear Engineering and Design, 313, 273-284.

Wu, Z., Laurence, D., Utyuzhnikov, S., & Afgan, I. (2019). Proper orthogonal decomposition and dynamic mode decomposition of jet in channel crossflow. Nuclear Engineering and Design, 344, 54-68.

Xiao, H., & Jenny, P. (2012). A consistent dual-mesh framework for hybrid LES/RANS modeling. Journal of Computational Physics, 231(4), 1848–1865. https://doi.org/10.1016/j.jcp.2011.11.009

Xiao, H., Wang, J.-X., & Jenny, P. (2014). Dynamic Evaluation of Mesh Resolution and Its Application in Hybrid LES/RANS Methods. Flow Turbulence Combust, 93(1), 141–170.

Xiao, H., Wang, J.-X., & Jenny, P. (2016). An Implicitly Consistent Formulation of a Dual-Mesh Hybrid LES/RANS Method. Commun. Comput. Phys, 1–30.

Yoshizawa, A., & Horiuti, K. (1985). A Statistically-Derived Subgrid-Scale Kinetic Energy Model for the Large-Eddy Simulation of Turbulent Flows. Journal of the Physical Society of Japan, 54(8), 2834–2839. https://doi.org/10.1143/JPSJ.54.2834

Zhang, Y., & Reese, J. M. (2003). Gas Turbulence Modulation in a Two-Fluid Model for Gas-Solid Flows. AIChE Journal, 49(12), 3048–3065. https://doi.org/10.1002/aic.690491207

Appendix A. The ''elliptic blending $k-\varepsilon-v^2/k$'' or the $BL\ v2/k$ model

- The elliptic blending parameter (α) equation:

$$\alpha - L^2 \boldsymbol{\nabla}^2 \alpha = 1 \tag{A.1}$$

$$L = \sqrt{{C_L}^2 \left(\frac{k^3}{\varepsilon_h^2} + {C_\eta}^2 \frac{\nu^{1.5}}{\varepsilon_h^{0.5}} \right)} \tag{A.2}$$

- Turbulent kinetic energy (k) equation:

$$\frac{Dk}{Dt} = P_k - \varepsilon_h + S_\varepsilon + \frac{\partial}{\partial x_j}\left(\left(\frac{\nu}{2} + \frac{\nu_t}{\sigma_k} \right) \frac{\partial k}{\partial x_j} \right) + G_k \tag{A.3}$$

$$P_k = \nu_t \langle S \rangle^2 \tag{A.4}$$

$$\langle S \rangle = \sqrt{2 \langle S_{ij} \rangle \langle S_{ij} \rangle} \tag{A.5}$$

$$\langle S_{ij} \rangle = 0.5 \left(\frac{\partial \langle U_i \rangle}{\partial x_j} + \frac{\partial \langle U_j \rangle}{\partial x_i} \right) \tag{A.6}$$

$$S_\varepsilon = -2 C_{\varepsilon 3} \nu_t \nu (1-\alpha)^3 \frac{k}{\varepsilon_h} \left(\frac{\partial^2 \langle U_i \rangle}{\partial x_j \partial x_k} \right)^2 \tag{A.7}$$

$$G_k = \beta g_i \frac{\nu_t}{Pr_t} \frac{\partial \langle T \rangle}{\partial x_i} \tag{A.8}$$

where β is the thermal expansion coefficient, g_i is the gravity vector and G_k represents the buoyancy production of k (the exact buoyancy production has a turbulent heat flux which was modelled here using the Standard gradient diffusion hypothesis).

- Homogeneous dissipation rate (ε_h) equation:

$$\frac{D\varepsilon_h}{Dt} = \frac{C_{\varepsilon 1} P_k - {C_{\varepsilon 2}}^* \varepsilon_h}{\tau} + \frac{\partial}{\partial x_j}\left(\left(\frac{\nu}{2} + \frac{\nu_t}{\sigma_\varepsilon} \right) \frac{\partial \varepsilon_h}{\partial x_j} \right) + {G_k}^\varepsilon \tag{A.9}$$

$${C_{\varepsilon 2}}^* = C_{\varepsilon 2} + \alpha^3 (C_{\varepsilon 4} - C_{\varepsilon 2}) tanh \left(\left| \frac{\frac{\partial}{\partial x_j}\left(\frac{\nu_t}{\sigma_k} \frac{\partial k}{\partial x_j} \right)}{\varepsilon_h} \right|^{\frac{3}{2}} \right) \tag{A.10}$$

where the buoyancy production of the turbulence dissipation rate (${G_k}^{\varepsilon}$) and the time scale τ read, respectively:

$$ {G_k}^{\varepsilon} = C_{\varepsilon 1} \frac{G_k}{\tau} \tag{A.11} $$

$$ \tau = \sqrt{\left(\frac{k}{\varepsilon_h}\right)^2 + {C_T}^2 \left(\frac{\nu}{\varepsilon_h}\right)} \tag{A.12} $$

- Turbulent viscosity (ν_t):

$$ \nu_t = c_\mu \varphi k \min(\tau, \tau_{\min}) \tag{A.13} $$

$$ \tau_{\min} = \frac{C_t}{\sqrt{3} c_\mu \varphi \langle S \rangle} \tag{A.14} $$

- Equation for the quantity $\varphi = \frac{\langle v^2 \rangle}{k}$ (where $\langle v^2 \rangle$ is the wall-normal Reynolds stress):

$$ \frac{D\varphi}{Dt} = (1 - \alpha^3) f_w + \alpha^3 f_h - P_k \frac{\varphi}{k} + \frac{\partial}{\partial x_j}\left(\left(\frac{\nu}{2} + \frac{\nu_t}{\sigma_\varphi}\right)\frac{\partial \varphi}{\partial x_j}\right) \tag{A.15} $$

$$ f_h = \frac{-1}{\tau}\left(C_1 - 1 + C_2 \frac{P_k}{\varepsilon_h}\right)\left(\varphi - \frac{2}{3}\right) \tag{A.16} $$

$$ f_w = \frac{-\varepsilon_h \varphi}{2k} \tag{A.17} $$

- The classic dissipation rate ε can be obtained from ε_h using:

$$ \varepsilon = \varepsilon_h + 0.5\, \nu \frac{\partial^2 k}{\partial x_j^2} \tag{A.18} $$

The formulation of the Reynolds stress tensor that was suggested by Sebilleau (2016) for use in the turbulent heat flux formulation when using the $BL\ v2/k$ model was utilised here to estimate $\langle u_i u_j \rangle$:

$$ \langle u_i u_j \rangle = \left[\frac{2}{3}\alpha^3 k \delta_{ij} - 2\nu_t \langle S_{ij} \rangle\right] + (1 - \alpha^3)\left[\varphi k n_i n_j + \frac{2}{3} k \left(\delta_{ij} - n_i n_j\right)\right] \tag{A.19} $$

It can be observed that the buoyancy production of φ which equals $-G_k \frac{\varphi}{k}$ was not added to Equation (A.15). The reason for this is that in the core of the cavity, this source term becomes positive as the buoyancy production G_k is negative in this region (because of the stable stratification). This can cause φ to increase until it becomes unbounded eventually resulting in solution divergence (this was encountered particularly in the hybrid RANS

simulations). Another remedy of this problem would be to clip G_k to 0 which is the approach adopted in Code_Saturne.

Another point worth noting is that the divergence of the φ equation was also encountered because of the fact that in the hybrid RANS simulations, the production term P_k is modified (see Equation (13)), which can cause P_k to become negative at some locations. To fix this problem P_k in the φ equation was clipped to 0 using $max(P_k, 0)$.

When attempting to replicate the RANS results produced here, attention should be paid to the version of the Elliptic blending $k-\varepsilon-v^2/k$'' model used. It has been observed that using a version similar to the one implemented in STARCCM+ v11.02 can yield different results. The difference mainly lies in that in STARCCM+ v11.02 the term S_ε, which gives additional dissipation in the buffer layer, is removed from the k equation and an equivalent term is included in the dissipation equation.

$C_{\varepsilon 1}$	$C_{\varepsilon 2}$	σ_k	σ_ε	σ_φ	c_μ
1.44	1.83	1	1.5	1	0.22
C_T	C_t	C_L	$C_{\varepsilon 3}$	$C_{\varepsilon 4}$	C_1
4	0.6	0.164	2.3	1	1.7
C_2	C_η				
0.9	75				

Table A.1. The $BL\ v2/k$ model constants.

Appendix B. The one-equation eddy viscosity LES model

$$\frac{\partial k_{sgs}}{\partial t}+\frac{\partial}{\partial x_j}\left(k_{sgs}\overline{U_j}\right) = 2\nu_{sgs}\overline{S_{ij}}^2+\frac{\partial}{\partial x_j}\left(\nu_{sgs}\frac{\partial k_{sgs}}{\partial x_j}\right) - \varepsilon_{sgs}+G_{ksgs} \tag{B.1}$$

$$\varepsilon_{sgs}=\frac{C_\varepsilon {k_{sgs}}^{3/2}}{\Delta} \tag{B.2}$$

$$\nu_{sgs}=C_k {k_{sgs}}^{1/2}\,\Delta\frac{\kappa}{C_\Delta}\left(1-y\,exp\left(-\frac{y^+}{A^+}\right)\right) \tag{B.3}$$

$$\overline{S_{ij}}=0.5\left(\frac{\partial\overline{U_i}}{\partial x_j}+\frac{\partial\overline{U_j}}{\partial x_i}\right) \tag{B.4}$$

where the filter width Δ was evaluated as the cubic root of the cell volume. C_k, C_ε, κ, A^+ and C_Δ are constants. It can be noticed that the ''van Driest damping function'' is included in the definition of the lengthscale used to estimate the modelled sgs viscosity ν_{sgs}. The buoyancy production term G_{ksgs} was calculated as:

$$G_{ksgs} = \beta g_i \frac{\nu_{sgs}}{Pr_{sgs}} \frac{\partial \bar{T}}{\partial x_i} \qquad \text{(B.5)}$$

As regards the boundary condition of ν_{sgs} at the walls, a zero gradient condition was used. However, the subgrid-scale diffusivity $\frac{\nu_{sgs}}{Pr_{sgs}}$ (which appears in the equations of the thermal field) was strictly set to 0 at the walls. Using a zero gradient or a fixed value of 0 for both quantities was found to yield rather poor pure coarse LES results for the square cavity flow. However, the hybrid method's results showed a weak sensitivity to the wall boundary condition of ν_{sgs} as the LES is forced towards the RANS in the near-well cells in the dual-mesh simulation.

C_k	C_ε	κ	A^+	C_Δ
0.094	1.048	0.41	26	0.158

Table B.1. The "one-equation eddy viscosity model" constants.

Appendix C. Results obtained with an LES zone weight (σ^L) based on Re_y

Before discussing the dual-mesh results, it is useful to look at the behaviour of the LES zone weight in a hybrid simulation in which it was calculated using Equation (8). In Fig. C.1, a contour plot of the LES zone weight from the hybrid simulation is shown. As can be seen from this figure, σ^L is equal to 0 not only near the cavity walls but also at other locations far from the walls. This can be clearly seen near the core of the cavity and can be explained by the fact that the flow is laminar in this region since the stable stratification destroys turbulence and as a result, the quantity Re_y becomes small (even though at the outside of the boundary layer the wall distance is relatively high, the low turbulence levels make the product $k^R y$ small and thus result in a small Re_y)[5]. In other words, the criterion provided by Equation (8) gives a σ^L of 0 near the wall and in the cavity core as it fails to distinguish between the laminarization that occurs in the near-wall region due to the no-slip and no-penetration conditions and the far-from-the-wall laminarization caused by the stable stratification.

[5] *At the outside of the boundary layer, k^R (which is a hybrid RANS variable) is forced towards k^{EWA} (which is a hybrid LES variable). Although k^{EWA} approaches 0 in this region, it is greater than the pure RANS turbulent kinetic energy in the same region. If one replaces k^R in Equation (8) with the pure RANS turbulent kinetic energy, a different behaviour of σ^L would be obtained.*

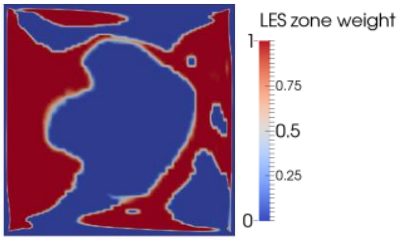

Fig. C.1. An instantaneous snapshot of the LES zone weight from a hybrid simulation in which it was calculated using Equation (8).

Small values of Re_y are also featured near the horizontal walls because these regions feature low turbulence levels. By looking at Fig. C.2 which shows time averaged values of σ^L, it can be seen that even with the time averaging, the behaviour of σ^L remains unsmooth.

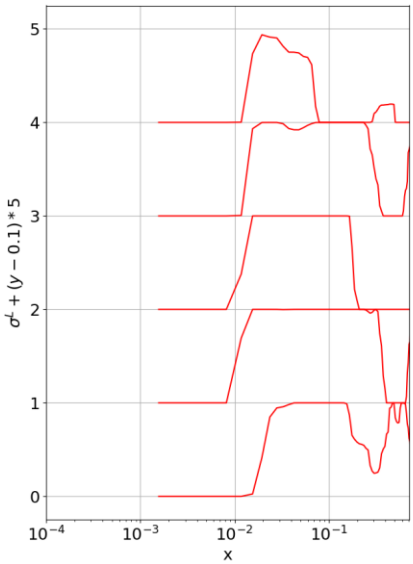

Fig. C.2. Mean values of the LES zone weight (σ^L) from a hybrid simulation in which it was calculated using Equation (8). This figure shows σ^L profiles at horizontal lines that correspond to cavity heights equal to $0.1H$, $0.3H$, $0.5H$, $0.7H$ and $0.9H$. The horizontal axis is in log scale.

One important thing to note is that when using the dual-mesh approach, what happens when σ^L is 0 in regions where the unstable plumes are forming in the LES simulation is that the velocity and temperature fluctuations associated with these plumes are altered since the LES fluctuations are forced towards the RANS fluctuations. This weakens the plume fluctuations, which in turn causes the turbulence levels along the vertical walls to be low. This can be seen from Fig. C.3 in which the velocity profiles returned by the hybrid method show an underestimation of the hot wall boundary layer thickness (due to less mixing taking place). This means one should

try and reduce the forcing of the LES towards the RANS near the regions where the LES unstable plumes are ejected by limiting the forcing as much as possible to the immediate near-wall region.

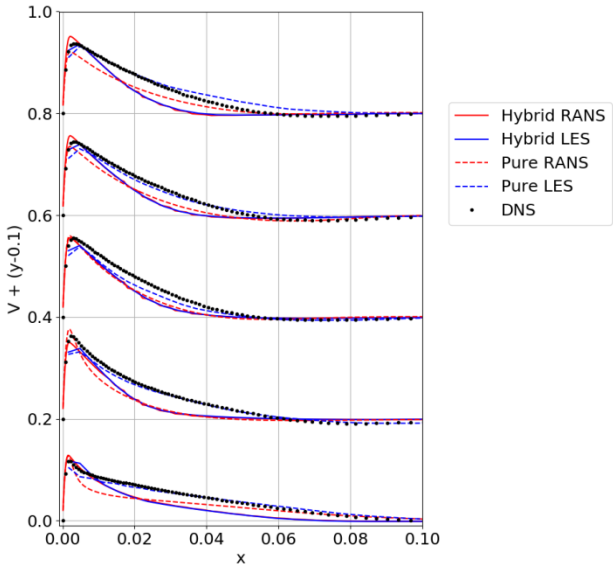

Fig. C.3. A plot showing the pure RANS, pure LES, hybrid RANS and hybrid LES predictions of the mean vertical velocity profiles near the hot wall at horizontal lines that correspond to cavity heights equal to $0.1H$, $0.3H$, $0.5H$, $0.7H$ and $0.9H$. In the hybrid simulations σ^{L} was calculated using Equation (8).

The weakening of the hybrid LES instability can be confirmed by looking at the temperature snapshot shown in Fig. C.4 and comparing the instability near the bottom left or top right corners with that of the pure coarse LES which can be visualized in Fig. 7. The drop in the turbulence levels along the hot wall in the hybrid LES simulation can also be confirmed by comparing the snapshots of the velocity magnitude taken from the hybrid LES and the pure coarse LES simulations (Fig. C.5 and Fig. 6, respectively). Indeed, the turbulent kinetic energy profiles plotted in Fig. C.7 clearly show that the turbulent mixing along the hot wall in the hybrid LES simulation is less than the one in the pure coarse LES. Fig. C.6 shows an instantaneous hybrid RANS temperature field in which the instability can be seen although it appears to be weaker than the pure RANS instability shown previously in Fig. 8.

Fig. C.4. An instantaneous snapshot of the LES temperature from a hybrid simulation in which the LES zone weight was calculated using Equation (8). A zoomed-in view of the contours near the bottom left corner is provided as well.

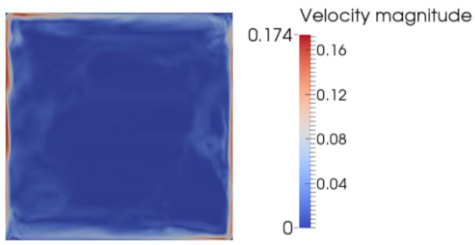

Fig. C.5. An instantaneous snapshot of the LES velocity magnitude from a hybrid simulation in which the LES zone weight was calculated using Equation (8).

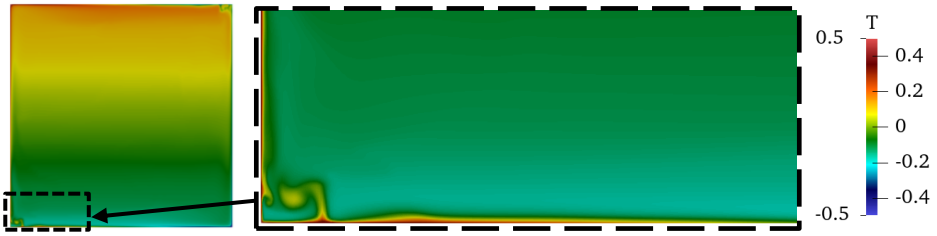

Fig. C.6. An instantaneous snapshot of the RANS temperature from a hybrid simulation in which the LES zone weight was calculated using Equation (8). A zoomed-in view of the contours near the bottom left corner is provided as well.

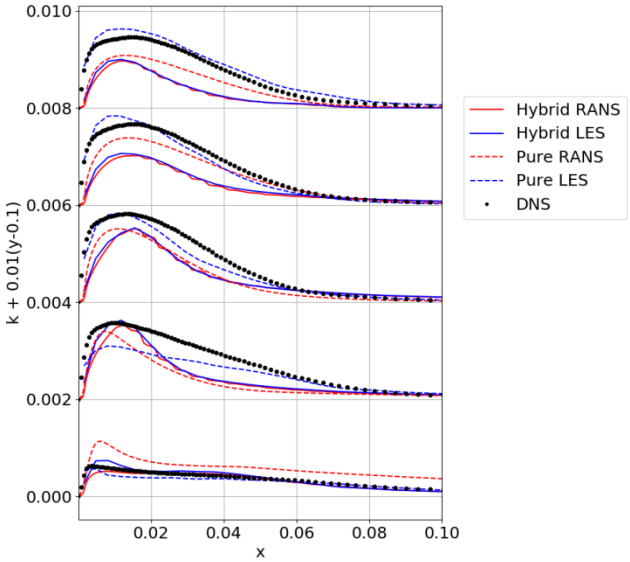

Fig. C.7. A plot showing the pure RANS, pure LES, hybrid RANS and hybrid LES predictions of the total turbulent kinetic energy profiles near the hot wall at horizontal lines that correspond to cavity heights equal to $0.1H$, $0.3H$, $0.5H$, $0.7H$ and $0.9H$. In the hybrid simulations σ^{L} was calculated using Equation (8).